Chalcogenide thermoelectrics empowered by an unconventional bonding mechanism

Original
Chalcogenide thermoelectrics empowered by an unconventional bonding mechanism / Yu, Y., Cagnoni, M., Cojocaru mirédin, O., Wuttig, M.. - In: ADVANCED FUNCTIONAL MATERIALS. - ISSN 1616-3028. - STAMPA. - 30:8(2020), pp. 1-19. [10.1002/adfm.201904862]

Publisher:
Wiley

Published
DOI:10.1002/adfm.201904862


ASTM D5946
ASTM D7334
ASTM D7490
ISO 27448


ASTM D1331
ASTM D1417
ISO 1409


ISO/TR 13097

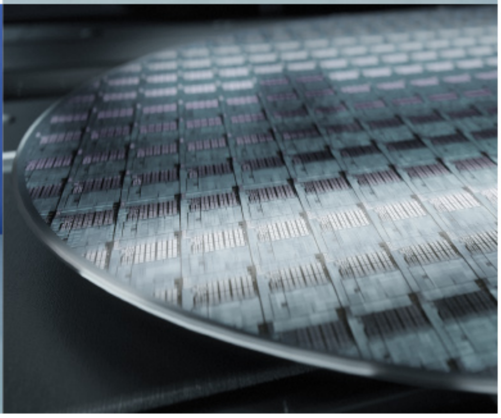

Chalcogenide Thermoelectrics Empowered by an Unconventional Bonding Mechanism

*Yuan Yu, Matteo Cagnoni, Oana Cojocaru-Mirédin, and Matthias Wuttig**

Thermoelectric materials have attracted significant research interest in recent decades due to their promising application potential in interconverting heat and electricity. Unfortunately, the strong coupling between the material parameters that determine thermoelectric efficiency, i.e., the Seebeck coefficient, electrical conductivity, and thermal conductivity, complicates the optimization of thermoelectric energy converters. Main-group chalcogenides provide a rich playground to alleviate the interdependence of these parameters. Interestingly, only a subgroup of octahedrally coordinated chalcogenides possesses good thermoelectric properties. This subgroup is also characterized by other outstanding characteristics suggestive of an exceptional bonding mechanism, which has been coined metavalent bonding. This conclusion is further supported by a map that separates different bonding mechanisms. In this map, all octahedrally coordinated chalcogenides with good performance as thermoelectrics are located in a well-defined region, implying that the map can be utilized to identify novel thermoelectrics. To unravel the correlation between chemical bonding mechanism and good thermoelectric properties, the consequences of this unusual bonding mechanism on the band structure are analyzed. It is shown that features such as band degeneracy and band anisotropy are typical for this bonding mechanism, as is the low lattice thermal conductivity. This fundamental understanding, in turn, guides the rational materials design for improved thermoelectric performance by tailoring the chemical bonding mechanism.

1. Introduction

More than two-thirds of energy generated is wasted in the form of low-grade heat, causing the ever-rising issue of environmental pollution.[1] Capturing and utilizing such a huge amount of heat could play an important role in building a sustainable society. Thermoelectric devices convert waste heat into electricity or pump heat by applying direct current without any compressive media and moving parts.[2,3] Hence, they can help to improve the efficiency of energy transformation processes. The thermoelectric energy conversion efficiency is determined by the dimensionless figure of merit, $zT = S^2\sigma T/(\kappa_e + \kappa_l)$, where S and σ are the Seebeck coefficient and electrical conductivity and their product $S^2\sigma$ is called power factor; T, κ_e, and κ_l are the absolute temperature, the electronic thermal conductivity, and the lattice thermal conductivity, respectively.[3–5] Yet, three of the quantities relevant for the conversion efficiency, i.e., S, σ, and κ_e are closely interwoven. Increasing one of them thus often has a detrimental effect on the others. Therefore, it is difficult to identify straightforward design rules to optimize thermoelectric materials. This has already been pointed out by Singh in the beginning of this century, when he commented "discovering a material with high thermoelectric figure of merit is akin to finding the proverbial needle in a haystack, because of seemingly contradictory requirements—high S like a semiconductor, high σ like a metal, and low thermal conductivity like a glass."[6] Yet, with persistent efforts, the number of thermoelectric materials has been greatly increased over the last two decades. These materials can be roughly categorized into three groups according to their temperature range of application. The low-temperature (<550 K) materials contain group-V alloys,[7] V_2VI_3,[8–12] $CsBi_4Te_6$,[13] and α-MgAgSb,[14] etc., in general exhibiting zT values below 1.5. The class of medium-temperature (550–950 K) materials contains many compounds, including IV–VI alloys, such as PbTe,[15,16] SnTe,[17] GeTe,[18] and SnSe,[19] I–V–VI_2 compounds,[20,21] Zintl compounds,[22] filled Skutterudites,[23] Clathrates,[24] Cu_2Se,[25] and BiCuSeO,[26] to name a few. They normally embrace maximum zT values above 1.5. The family of high-temperature (>950 K) thermoelectrics is smaller, encompassing materials such as SiGe,[27] $La_{3-x}Te_4$,[28] and half-Heusler alloys.[29] They all show maximum zT values close to 1.

Chalcogenide (group VI) compounds consisting in addition of group-IV and group V elements are semiconductors or semimetals which find applications in phase change memory,[30,31] as a topological insulator,[32] and in

---

Dr. Y. Yu, Dr. M. Cagnoni, Dr. O. Cojocaru-Mirédin, Prof. M. Wuttig
I. Physikalisches Institut (IA)
RWTH Aachen University
Sommerfeldstraße, 52074 Aachen, Germany
E-mail: wuttig@physik.rwth-aachen.de

Prof. M. Wuttig
JARA-Institut Green IT
JARA-FIT
Forschungszentrum Jülich GmbH and RWTH Aachen University
52056 Aachen, Germany

The ORCID identification number(s) for the author(s) of this article can be found under https://doi.org/10.1002/adfm.201904862.

DOI: 10.1002/adfm.201904862

thermoelectric energy conversion,[3,4,33] etc. For applications in thermoelectric energy converters, chalcogenides embrace many advantages. First, most of them can easily be doped into p-type or n-type, which is critical for the assembly of thermoelectric devices.[15–18,34–36] Second, they consist of heavy elements and soft chemical bonds, resulting in low thermal conductivity.[3,12,16–18] Third, they possess a variety of structures, providing a good platform for manipulating the thermoelectric performance. At ambient temperature and pressure, they often reveal one of three different crystal structures: rock-salt NaCl type, e.g., PbTe, rhombohedral grey-As type, e.g., GeTe, and orthorhombic black-P type, e.g., SnSe (see also Figure 5a). All of these structures are characterized by an octahedral-like atomic arrangement. Fourth, they possess a low operating cost, beneficial for wide-range applications.[37] These compounds dominate thermoelectric applications in the low to medium temperature range. V_2VI_3 compounds, for example, have been used commercially as thermoelectric coolers since the 1950s.[9,38] The medium temperature IV–VI compounds provide a playground to manipulate the thermoelectric properties by band engineering and hierarchical structure phonon scattering, leading to the enhancement of zT from nearly 1 to above 2. For instance, p-type PbTe shows a maximum zT of ≈2.6 at 850 K,[39] while p-type GeTe possesses a maximum zT of 2.4 at 600 K,[40] p-type SnSe single crystals show a zT of 2.6 at 923 K,[41] and n-type SnSe single crystals show a zT of 2.8 at 773 K.[35] Some rare-earth chalcogenides can even be used above 1000 K due to their high thermal stability, such as $La_{3-x}Te_4$ which exhibits a maximum zT of ≈1.1 at 1275 K.[28] More comprehensive discussions of the thermoelectric properties of chalcogenide compounds can be found elsewhere.[4,15–18,42,43]

In the last twenty years, many new thermoelectric materials have been proposed, along with guidelines to help their discovery. Yet, finding a high zT material still remains quite cumbersome, possibly because of the lack of clear rules to assist their search. Hence, in this review, an alternative approach to the identification of thermoelectrics is presented, focusing on main-group chalcogenides. A chemical bonding perspective will be developed, in which the superior performance of chalcogenide based thermoelectrics is attributed to an unconventional bonding mechanism. To this end, first different properties for a significant number of chalcogenides are presented. All chalcogenides with a large thermoelectric figure of merit have an unconventional portfolio of properties. Such a combination of properties is not found for similar chalcogenides, which possess a low figure of merit. This indicates that the materials with superior performance as thermoelectrics might employ an exceptional bonding mechanism. This bonding mechanism is presented next. Subsequently, the question is addressed, if this bonding mechanism can explain features, which have been proven to be crucial to reach high values of zT, such as the band degeneracy and the band anisotropy, or the low lattice thermal conductivity. Finally, a possible route for the guided discovery of materials with exceptional thermoelectric performance utilizing maps for chemical bonding is presented.

To understand the origin of the excellent thermoelectric performance of some of these chalcogenides, relevant electronic and thermal transport properties, as well as intrinsic physical parameters, are summarized for many chalcogenides in **Table 1**.

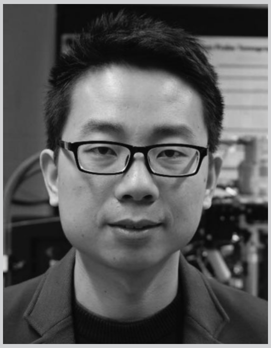

Yuan Yu received his Ph.D. degree in materials science and engineering from Hefei University of Technology in 2017. He was a visiting student at the Institute of Physics of RWTH Aachen University in Germany from November 2015 to May 2017. After obtaining his Ph.D. degree, he joined Prof. Matthias Wuttig's group as a postdoctoral researcher. His primary scientific interests include the characterization and understanding of thermoelectric materials and phase change materials using (transmission) electron back-scatter diffraction and atom probe tomography.

Oana Cojocaru-Mirédin received her Ph.D. degree in physics in 2009 from the University of Rouen, France, with the "Group Physique des Matériaux" laboratory, well-known for their development of the APT technique. Afterwards, she worked as a postdoc and then as Group Leader of the "Interface Design in Solar Cells" group with the Max-Planck-Institut für Eisenforschung. Currently, she is the head of the "Nanocharacterization of Advanced Functional Materials" group with the I. Institute of Physics, RWTH Aachen. Her research interests include the characterization and processing of semiconductors for photovoltaic and microelectronics applications by means of APT and TEM.

Matthias Wuttig received his Ph.D. in Physics in 1988 from RWTH Aachen/Forschungszentrum Jülich. He was a visiting professor at several institutions including Lawrence Berkeley Laboratory, Stanford University, Hangzhou University, IBM Almaden, Bell Labs, DSI in Singapore and the Chinese Academy of Sciences in Shanghai. In 1997, he was appointed Full Professor at RWTH Aachen. Since 2011, he heads a collaborative research center on resistively switching chalcogenides (SFB 917), funded by the DFG.

Table 1. Electronic and thermal transport properties for undoped chalcogenides as well as some specific values describing the band structure of chalcogenide thermoelectric compounds. $zT_{\max}$ describes the maximum zT value obtained at temperature T, p-type or n-type conduction is also provided, n is the carrier concentration, σ is the electrical conductivity, B is the bulk modulus, Θ_D is the Debye temperature, κ_l is the lattice thermal conductivity, E_g is the bandgap. Data unavailable from the literature are indicated by a backslash. References are given in Table S1 in the Supporting Information.

Material	$zT_{\max}$ @ T	Type	n [cm^{-3}]	σ [S cm^{-1}]	B [G Pa]	Θ_D [K]	κ_l [W (mK)$^{-1}$]	E_g [eV]
GeSe	0.05 @ 710 K	P	10^{14}	1.3×10^{-6}	47.5	280	3.0	1.1
α-GeTe	1.0 @ 673 K	P	10^{21}	5.0×10^{3}	49.9	199	2.6	0.1
β-GeTe	0.8 @ 723 K	P	10^{21}	6.8×10^{3}	51	157	1.5	0.36
SnS	0.1 @ 750 K	P	10^{17}	3.4×10^{-4}	47.6	270	2.0	1.16
α-SnSe	0.2 @ 600 K	P	10^{18}	2.5×10^{-5}	50.3	210	0.7	0.86
β-SnSe	2.6 @ 923 K	P	10^{19}	100	40.9	–	0.3	0.39
SnTe	0.7 @ 900 K	P	10^{20}	9.8×10^{3}	42	140	2.9	0.19
PbS	0.3 @ 773 K	N	10^{18}	260	50.2	227	2.56	0.41
PbSe	1.0 @ 700 K	P	10^{18}	400	47	170	1.53	0.28
PbTe	1.3 @ 700 K	P	10^{19}	2.9×10^{3}	41	130	2.1	0.3
β-As_2Te_3	0.56 @ 423 K	P	10^{19}	650	53.2	257.9	0.9	0.24
Sb_2S_3	–	–	–	1.0×10^{-8}	75.1	364.4	1.3	1.88
Sb_2Se_3	0.1 @ 673 K	N	10^{14}	4.0×10^{-7}	58.7	262.8	0.97	1.17
Sb_2Te_3	0.45 @ 547 K	P	10^{20}	2.3×10^{3}	44.8	160	1.75	0.11
Bi_2S_3	0.03 @ 673 K	N	10^{16}	9.4×10^{-7}	67.8	283	1.0	1.35
Bi_2Se_3	0.4 @ 600 K	N	10^{18}	1.0×10^{3}	48.4	205	1.3	0.25
Bi_2Te_3	0.7 @ 300 K	P	10^{19}	660	37.4	155	1.18	0.13
$AgSbSe_2$	0.4 @ 573 K	P	10^{18}	5	78	143	0.3	0.7
$AgSbTe_2$	1.2 @ 600 k	P	10^{19}	325	67	125	0.68	0.35
$AgBiS_2$	0.03 @ 400 K	N	–	1.0×10^{-3}	62	–	0.65	0.8
$AgBiSe_2$	0.5 @ 773 K	N	10^{19}	180	74	135	0.64	0.52
$AgBiTe_2$	–	N	–	1.3×10^{3}	66	–	0.9	0.16

All chalcogenides listed in this table share an octahedral-like arrangement of the atoms (see also Figure 5a), yet with varying levels of distortions. Interesting enough, these materials can be divided into two groups regarding their performance as thermoelectrics. This can be seen best when comparing a number of isoelectronic pairs, such as GeTe and GeSe, or Bi_2Se_3 and Bi_2S_3. While GeTe reveals a maximum zT of 1.0 at 673 K,[44] GeSe shows a zT of 0.05 at 710 K.[45] A similar observation can be made upon comparing Bi_2Se_3 with Bi_2S_3, which differ by more than a factor of 10 in zT.[46,47] Such pronounced differences for isoelectronic materials are striking and call for an explanation. Remarkably, the two pairs of materials (GeTe and Bi_2Se_3/GeSe and Bi_2S_3) do not only differ in their thermoelectric performance, but they also differ in their physical properties. All materials with a high thermoelectric figure of merit possess a rather low Debye temperature, as displayed in **Figure 1**a,b. This is not particularly surprising since the materials with a large figure of merit are also those which tend to have heavier atoms, leading to low phonon frequencies and hence low Debye temperatures. Low phonon frequencies are beneficial in realizing a low thermal conductivity for the phonons, one of the requirements for good thermoelectrics. Yet, there are also other physical properties that differ significantly from those of their less efficient thermoelectric counterparts. Bi_2Se_3, for example, has a significantly larger electrical conductivity and lower bandgap than its isoelectronic relative Sb_2Se_3, as depicted in Figure 1c,d. Other properties of these two materials differ considerably, too. These differences apparently hold for all members of the subgroup of efficient thermoelectric chalcogenides listed in Table 1. All materials with a zT above 0.25 in Table 1 are characterized by a large carrier concentration and rather high electrical conductivity, small Bulk modulus, low Debye temperature, low lattice thermal conductivity, and a small bandgap which satisfies the requirement of ≈6–10 k_BT for good thermoelectrics.[48] Hence, these materials combine all attributes desirable for thermoelectric materials. They also possess a property combination which is rather exceptional and is found in none of the materials employing covalent, ionic, or metallic bonding. This unconventional property combination has recently been attributed to a special bonding mechanism, coined metavalent bonding.[49,50] Yet, for the present purpose it is not relevant if the bonding in chalcogenides is a novel bonding mechanism, or a strange mixture of known bonding mechanisms. Instead, two questions are crucial to identify novel thermoelectrics with superior performance based on chalcogenides. (a) How can the properties which are desirable for applications as thermoelectrics be related to the exceptional property portfolio and hence bonding of these chalcogenides? (b) How can chalcogenides be identified that have this unconventional property combination?

To this end, the unique property combination will be discussed and related to potential bonding mechanisms in solids.

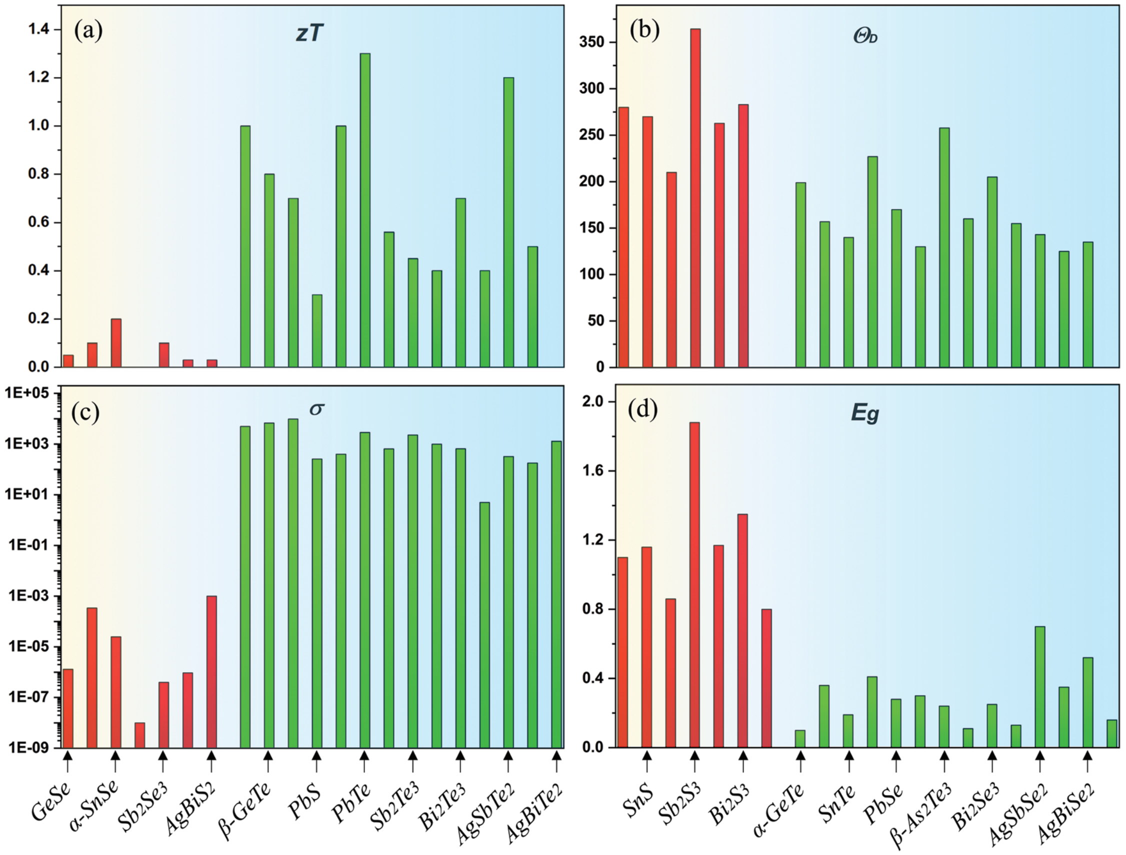

Figure 1. Characteristic properties of pristine chalcogenide compounds listed in Table 1. a) Maximum zT values; b) Debye temperature in Kelvin; c) Electrical conductivity at room temperature in S cm^{-1}; d) Bandgap in eV. These materials can be divided into two groups regarding their performance as thermoelectrics: materials with zT values larger than 0.25 are displayed in green, while those with zT below 0.25 are depicted in red. The subgroup which possesses high figure of merits also shows a distinct property portfolio, including a low Debye temperature, high electrical conductivity, and small bandgap.

Subsequently, the characteristic properties of thermoelectrics will be related to the bonding mechanism and accompanying properties prevalent in chalcogenides suitable for thermal energy conversion. Finally, it will be discussed, how materials can be identified that combine the desired properties, aiding the search of novel thermoelectrics based upon clear design rules.

2. Metavalent Bonding

Five fundamental bonding mechanisms, including metallic, covalent, and ionic bonding, as well as the two weaker forms of hydrogen and van der Waals bonding, have been recognized as iconic bonding mechanisms in solids. Metallic bonding is closely related to electron delocalization of the conductance electrons over several neighbors, resulting in high electrical and thermal conductivity. Metals lack a bandgap, which leads to their mirror-like finish when polished. Covalent bonding is formed by sharing electron pairs between atoms. These electron pairs are located between adjacent atoms forming either σ-bonds or π-bonds. Covalently bonded materials usually possess a bandgap and an electrical conductivity much lower than that of metals (if they have not been doped). Ionic bonding involves the electrostatic attraction between oppositely charged ions (cation and anion), originating from a transfer of electrons from cations to anions. This leads to very low levels of electrical conductivity and large bandgaps. Yet, it is important to remember that covalent and ionic bonding as discussed above are idealized limiting cases. Materials like ZnO or GaN will both have covalent and ionic bonding contributions. Unlike the covalent and ionic bonds, the van der Waals forces do not result from a transfer or significant sharing of electrons between adjacent atoms. It is hence comparatively weak. Each bonding mechanism leads to characteristic physical properties. The chalcogenides in Table 1, which show zT values above 0.25 possess a unique property portfolio.[3,31] For example, PbTe, SnTe, and GeTe exhibit moderate electrical conductivities, high optical dielectric constants (ε_∞) and hence a small bandgap E_g, large Grüneisen parameters for transverse optical modes (γ_{TO}), high Born effective charges (Z^*), and large effective coordination numbers (ECoN) incompatible with the "8–N" rule.[49] This combination of properties is neither observed for metallic, ionic, or covalently bonded materials. It will be shown below, how these characteristics, which are closely related with the bonding in solids can explain the favorable performance of certain chalcogenides in thermoelectric energy converters and how similar and possibly even superior compounds can be identified using maps.

In recent years, quantum chemical tools have been developed that enable characterization of bonding in solids based

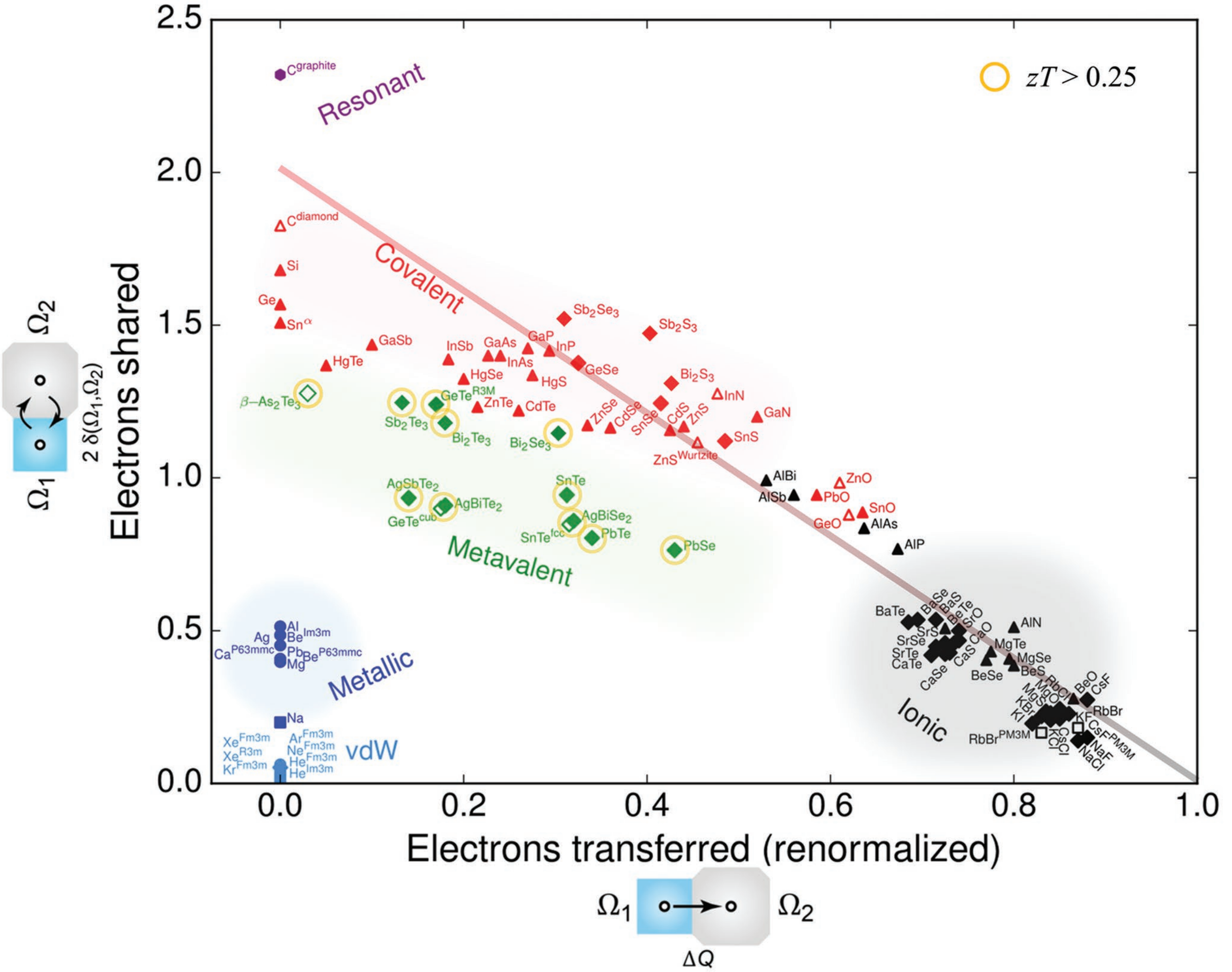

Figure 2. A 2D map of electronic interactions and bonding in materials. The amount of relative electrons transferred (x-axis) and shared between neighboring basins (y-axis) is computed using quantum-topological methods. Please note that the number of electrons transferred has been divided by the formal oxidation state to obtain the relative charge transfer. A relative electron transfer of 1 thus corresponds to the transfer of one electron in NaCl but two electrons in MgO. The different colors denote that the corresponding materials have different properties (structure, electrical conductivity, optical dielectric constant, anharmonicity, and bond polarizability) which are indicative for different bonding mechanisms, i.e., ionic (black), covalent (red), metallic (blue), van der Waals (light blue), and resonant bonding as in graphite or benzene (purple). Materials with an unconventional property portfolio (high values of ε_∞, an intermediate electrical conductivity, large anharmonicities, pronounced electron–phonon coupling, and an effective coordination number incompatible with ordinary covalent bonding) are denoted in green. Their properties have been attributed to an unconventional bonding mechanism which has been coined metavalent bonding. Interestingly, all octahedrally coordinated chalcogenides with a zT above 0.25 for their intrinsic phases are located in the green region. This implies that there could be a correlation between their thermoelectric performance and the bonding mechanism utilized. The map can be employed to identify novel thermoelectrics.

on the analysis of the Schrödinger equation. To this end, at first, the wave function of the electrons in the crystalline solid is calculated. Subsequently, quantum chemical tools[50,51] are employed to determine the charge transfer as well as the formation of electron pairs between adjacent atoms. Results of such calculations for a variety of solids are depicted in **Figure 2**. As the y-axis, the number of electrons shared between two adjacent atoms is depicted. The values displayed are twice the number of electron pairs formed between adjacent atoms, i.e., this is a two-electron quantity. Electron pair formation is the hallmark of covalent bonding, consistent with the data displayed in Figure 2. Elements like carbon (diamond), silicon, or germanium employ covalent bonding and are characterized by about two electrons between adjacent atoms, in line with the ideas of Gilbert Lewis for covalent bonding.[52] Ionic bonding, on the contrary, is characterized by electron transfer. The electron transfer for NaCl, for example, is 0.87 e, in line with chemical intuition. For MgO, an electron transfer of 1.70 e is calculated, again compatible with the idea of the formation of Mg^{2+} and O^{2-}. Hence, the absolute charge transfer in MgO is hence about twice as large as for NaCl, due to the difference in the oxidation state of the ions involved. To obtain a definition of charge transfer which is independent of the oxidation state, and can hence also be employed for SiO_2 or Sb_2Te_3, the x-axis in Figure 2 displays the relative electron transfer, i.e., the electron transfer divided by the formal oxidation state. As shown in this figure, covalent and ionic bonding occupy different corners of the map. Covalent bonding is located in the upper left corner, while materials with ionic bonding are found in the lower right corner. There exists a continuous transition from covalent to ionic bonding and vice versa; hence, materials like ZnO or GaN are both characterized by electron transfer (ionic bonding) and electron sharing (covalent bonding). The advantage of Figure 2 is that it depicts both quantities and thus enables an estimate of how covalent/ionic the bonding is. Furthermore, one can connect the two extremes, i.e., covalent bonding: no electron transfer, but formation of an electron pair, i.e., two electrons shared, and ionic bonding: no electron pair formation, but transfer of all valence electrons of the cation. The line connecting these points is depicted in Figure 2. Most materials in the map are either close to or below the line. This demonstrates a conventional wisdom, the valence electrons employed to bond adjacent atoms can only be shared or transferred. The map also depicts two other well-known bonding mechanisms, metallic and van der Waals bonding. In these two cases, there is minor or marginal electron transfer. In van der Waals bonding, there is in addition a minor amount of electrons shared between adjacent atoms. This is indicative for a very weak bond in line with chemical intuition since there is neither charge transfer nor significant sharing of electrons. Metallic bonding has a larger electron sharing than van der Waals bonding, but is far away from the limiting case of two electrons between adjacent atoms, encountered for covalent bonding. Sodium (Na), for example, is characterized by a sharing of 0.25 e between adjacent atoms. This result is easy to understand. Na has eight nearest neighbors. Hence, a Na atom can form an electron pair with an adjacent atom, but has eight such neighbors, giving rise to 2/8, i.e., 0.25 e per nearest neighbor, as shown in Figure 2.

Interestingly, all chalogenides with an octahedral-like atomic arrangement that possess a zT above 0.25 are located in a well-defined region of the map, where materials utilize an exceptional bonding mechanism. This seems to imply that we are not "searching for a needle in the haystack," but for materials with this unusual bonding mechanism. The map can thus be employed to identify materials which could have a good thermoelectric performance. Nevertheless, there is a second interesting usage of the map in Figure 2. One can combine this map with a third dimension which depicts a physical property which characterizes either features related to bonding (Born effective charge Z^*, optical dielectric constant ε_∞, ECoN, anharmonicity) or a characteristic, which is related to their thermoelectric performance such as the thermal or electrical conductivity. This is done in **Figure 3**, which reveals interesting property correlations.

The data depicted in Figure 3 provide further evidence for a relationship between the existence of an unusal bonding mechanism for a vast number of octahedral-like chalcogenides and their application potential as thermoelectrics. So far, evidence has been presented that the bonding mechanism in these chalcogenides is neither metallic, covalent, or ionic bonding, but a distinctively different bonding mechanism instead. Clearly, such a statement calls for further evidence to validate the claim of a novel bonding mechanism.

Indeed, a study of bond breaking using atom probe tomography[53,54] supports the idea of an exceptional bonding mechanism. To this end, laser-assisted atom probe tomography has been utilized to study bond rupture.[55] In an ideal case, the atoms on the specimen's surface will be ionized and evaporated successively triggered by the laser pulse. Each successful laser pulse, applied under well-controlled conditions, normally generates the evaporation of one ion, which is called a single event. However, in some cases, one single pulse induces the evaporation of multiple ions, which is termed as multiple events. The ratio between multiple events and total events is called the "probability of multiple events." By analyzing more than 50 different compounds, Zhu et al.[55] found that the "probability of multiple events" for metavalently bonded materials is larger than 50%, while the value for all covalent and metallic materials studied is lower than 40% with the same measurement parameters, **Figure 4**. The chalcogenides which show superior performance as thermoelectric materials, do not only show an exceptional property portfolio, they are also characterized by an unconventional bond breaking mechanism. Hence, in Figure 2, all chalcogenides from Table 1 with a zT value above 0.25 are marked with yellow circles. Indeed, all chalcogenides with obvious potential as a thermoelectric are depicted in a well-defined area of the map, which has been identified as the region of metavalently bonded materials.

One can now raise the question, how an unconventional bonding mechanism could be related to the desired property portfolio of thermoelectrics. Is this relationship a mere coincidence or is it sign for a correlation or even a causality? In the following, we will try to understand the thermoelectric performance of chalcogenides from a chemical bonding perspective. We will first summarize the strategies for enhancing the power factor, especially band structure engineering including band convergence and band anisotropy. This will enable us to relate the unconventional bonding mechanism to a band structure which is conducive to good thermoelectric performance. We then discuss the intrinsically low lattice thermal conductivity arising from the soft chemical bonds and large anharmonicities.

3. Intrinsic Defects and Carrier Concentration

To optimize the thermoelectric performance, the position of the Fermi energy is critical. On the one hand, the Fermi level should be deep in the bands to increase the electrical conductivity. On the other hand, as the Fermi level moves deeper into the bands, charge carriers below the Fermi level compensate the entropy transported by carriers above the Fermi level. This decreases the Seebeck coefficient, which represents the average entropy carried per charge carrier.[56] The position of the Fermi level depends upon the carrier concentration, which can be easily measured. It can be tuned by alloying or doping. The optimum carrier concentration for thermoelectric materials lies in the range from 10^{18} to 10^{21} cm^{-3}.[3–5] Table 1 shows that the chalcogenides with good thermoelectric efficiency exhibit a high carrier concentration, which frequently lies in or close to the optimal range. Interestingly, the high carrier concentration of these chalcogenides is a generic feature of the undoped compound, i.e., it is a characteristic of the material. This raises the question, how the large number of charge carriers can be explained. They are frequently induced by cation vacancies, whose formation is apparently energetically feasible. This can be understood from a crystal orbital Hamilton population (COHP) analysis, which dissects the interactions of valence orbitals into bonding (stabilizing) and antibonding (destabilizing) states.[57] This analysis shows that the states close to the Fermi level are predominantly p-states. These p-states form σ-bonds between nearest neighbors (**Figure 5**b), giving rise to an octahedral-like atomic arrangement, as shown in Figure 5a. The p-states are half-filled, since they are occupied by an average of three p-electrons per lattice site.[58,59] Without charge transfer between the atoms or alternatively a distortion away from a simple cubic situation, we expect a metallic ground state (green curve in Figure 5d). A Peierls distortion or a small charge transfer between the atoms opens a small bandgap. (Figure 5c,d).

Figure 6 shows the COHP analyses of Ge–Sb–Te phase change materials which can also be good thermoelectrics.[59,61] By assuming a fully occupied sublattice, i.e., $Ge_2Sb_2Te_4$, the COHP analysis shows strong antibonding interactions at the Fermi level, as indicated by the red arrow. This is not surprising, since in $Ge_2Sb_2Te_4$ an average of 3.25 p-electrons occupies the lattice sites, leading to a population of antibonding states. These antibonding states at the Fermi level are indicative of an electronic and hence structural instability. To alleviate this unfavorable situation, the system removes cations, i.e., it forms cation vacancies. The COHP analysis of the vacancy-containing system, $GeSb_2Te_4$, shows that forming Ge vacancies indeed lowers the Fermi level and depopulates the antibonding states, as indicated by the black arrow in Figure 6. Note that the unoccupied antibonding states above the Fermi level do not lead to an instability of the system; it is only the occupied states that matter. A similar large population of occupied antibonding states has also been observed in GeTe,[62] rock-salt GeSe,[63] and Sb_2Te_3,[64] while they are not relevant for CaTe, CdTe, and orthorhombic GeSe, etc.[63] Hence, the depopulation of antibonding states is caused by cation vacancy formation, which creates holes in the valence band and hence p-type conductivity,

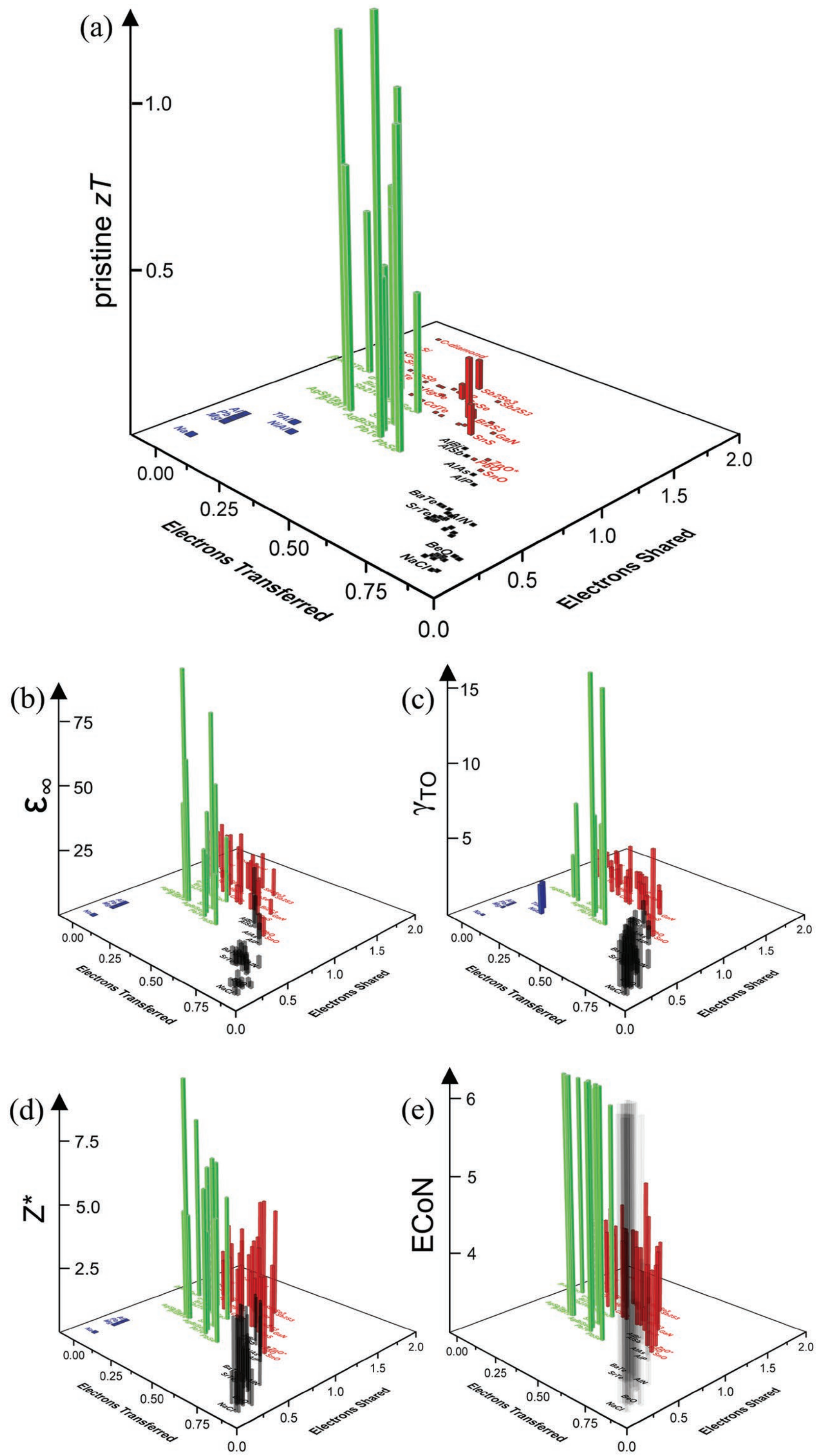

Figure 3. 3D maps showing the zT value of different intrinsic materials, prior to doping with foreign elements as well as other bonding-related properties for more than 80 compounds adopting different bonding mechanisms. a) zT value; b) optical dielectric constant, ε_∞, as an optical identifier of chemical bonding; c) transverse optical mode Grüneisen parameter, γ_{TO}, identifies the anharmonicity of the material; d) Born effective charge, Z^*, identifies the chemical bond polarizability; e) Effective coordination number, ECoN, as a structural identifier of chemical bonding. The numerical values for the different entries are collected in Table S1 (Supporting Information) and in ref. [50].

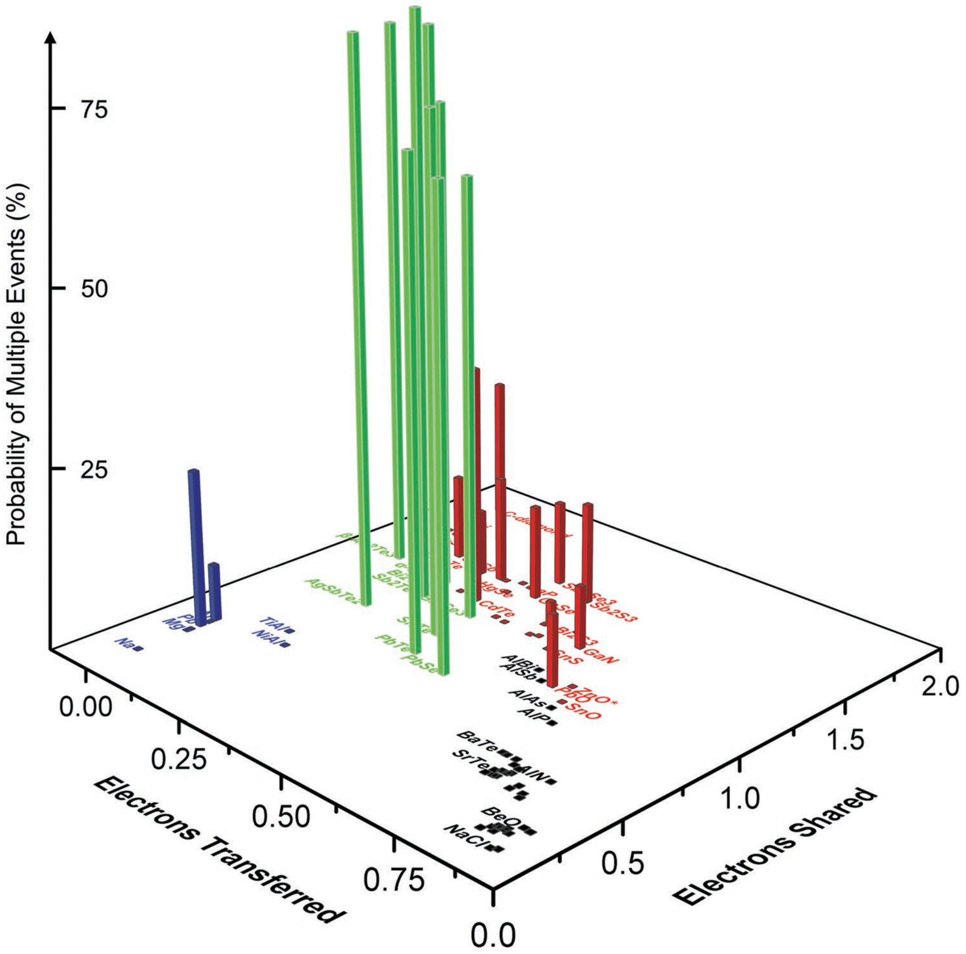

Figure 4. A 3D map using the basal plane of electrons transferred and electrons shared showing the "probability of multiple events" (PME) measured by laser-assisted atom probe tomography. All compounds with a high probability of creating several fragments upon exposure to a single laser pulse are located in the green area of the map, which is characterized by unconventional physical properties. In the green region, the probability of multiple events ranges from about 60% to more than 80%, while the highest value observed outside this region is about 33%. There is thus apparently a correlation between the thermoelectric performance and the bond breaking as measured by the atomprobe, as well as the material properties (see Table S1 (Supporting Information) and ref. [55] for details).

as observed for many chalcogenides with good thermoelectric properties (see Table 1).

4. Band Engineering by Tuning the Chemical Bond

Charge carriers distribution function and scattering mechanisms determine the electrical transport properties. For degenerate semiconductors and metals, the Mott expression gives the Seebeck coefficient S as[65]

$$S = \frac{\pi^2}{3}\frac{k_\mathrm{B}}{e}k_\mathrm{B}T\left\{\frac{1}{n}\frac{\mathrm{d}n(E)}{\mathrm{d}E}+\frac{1}{\mu}\frac{\mathrm{d}\mu(E)}{\mathrm{d}E}\right\}_{E=E_\mathrm{F}} \tag{1}$$

where k_B is the Boltzmann constant, e is the electron charge, μ is the carrier mobility, and E_F is the Fermi energy. The first term in brackets is related to the energy-dependence of density of states (DOS), while the second term is related to the energy-dependence of the carrier scattering. The latter can be optimized to favor a large Seebeck coefficient by enhancing scattering with ionized impurities,[66] or by energy filtering at grain boundaries.[67] In this review, the former is discussed. In particular, we will provide a chemical-bonding perspective on its optimization for maximum thermoelectric performance.

The first step is defining the three different effective masses relevant for the description of charge transport in the parabolic-band approximation. They are the DOS effective mass, m_d^*, the band effective mass, m_b^*, and the conductivity effective mass, m_σ^*. For a system with isotropic structure, they have the following relationships[4,5]

$$m_\mathrm{d}^* = (N_\mathrm{V})^{2/3}m_\mathrm{b}^* \tag{2}$$

$$m_\mathrm{b}^* = \left(\left(m_\perp^*\right)^2 m_\parallel^*\right)^{1/3} \tag{3}$$

$$m_\sigma^* = 3\left(\frac{2}{m_\perp^*}+\frac{1}{m_\parallel^*}\right)^{-1} \tag{4}$$

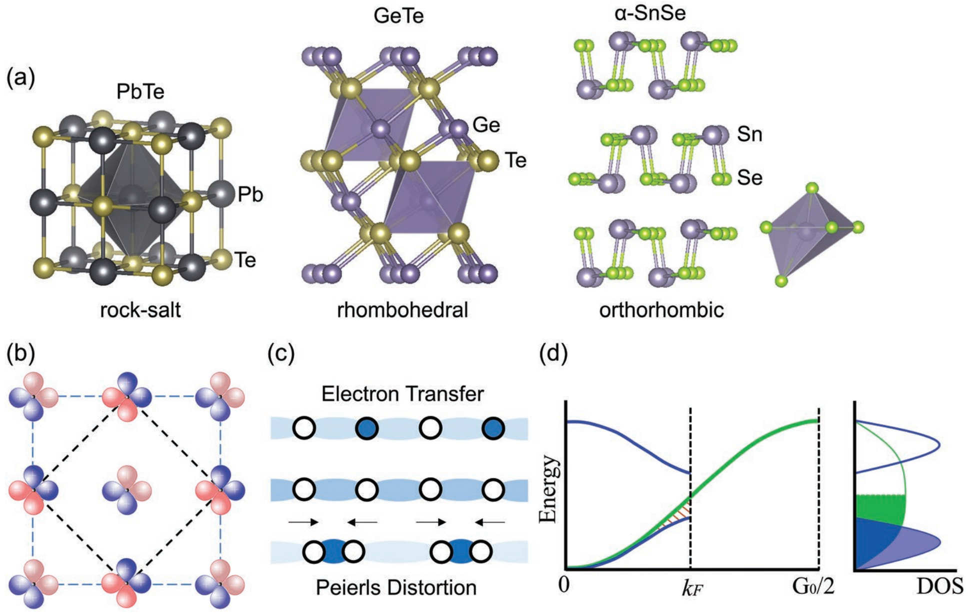

Figure 5. a) Octahedral-like coordination in PbTe, GeTe, and α-SnSe; b) Schematic diagram of the (001) plane of PbTe, displaying the σ-bonds formed from p-orbitals, which are responsible for the octahedral-like atomic arrangement; c) The middle sketch shows the symmetric atomic arrangement without charge transfer, while the distribution of electrons changes either by a Peierls distortion (bottom) or electron transfer (top); d) Density of states for the symmetric case (green) and a situation with a Peierls distortion or alternatively charge transfer between the atoms leading to bandgap opening (blue curve). Insets (c) and (d) are reproduced with permission.[60] Copyright 2011, WILEY-VCH.

where N_V is the band degeneracy, $m_\perp^*$ is the transverse effective mass, and $m_\parallel^*$ is the longitudinal effective mass.

As long as the scattering rate does not vary significantly on an energy scale of a few k_BT, a constant relaxation time approximation can be adopted.[68] Then, the Seebeck coefficient can be written as[69]

$$S = \frac{4^{1/3}\pi^2 k_B^2}{eh^2} m_d^* T \left(\frac{4\pi}{3n}\right)^{2/3} \tag{5}$$

while the electrical conductivity can be expressed as

$$\sigma = -en\mu \tag{6}$$

where the carrier mobility μ is related to the charge carrier relaxation time, τ, and the conductivity effective mass

$$\mu = e\tau / m_\sigma^* \tag{7}$$

These equations demonstrate that the electronic properties depend upon the effective mass tensor, the band degeneracy and the carrier relaxation time.

4.1. Band Degeneracy

According to Equations (2) and (7), band degeneracy is an independent parameter to modify the DOS effective mass without affecting the carrier mobility, if the intervalley scattering is negligible. Band degeneracy increases when multiple bands have similar energy within a few k_BT near the Fermi level. Large band degeneracy is found in materials with highly-symmetric crystal structures, but carrier pockets located at low-symmetry points of the Brillouin zone.[70] Alternatively, changing chemical composition or temperature can lead to the convergence

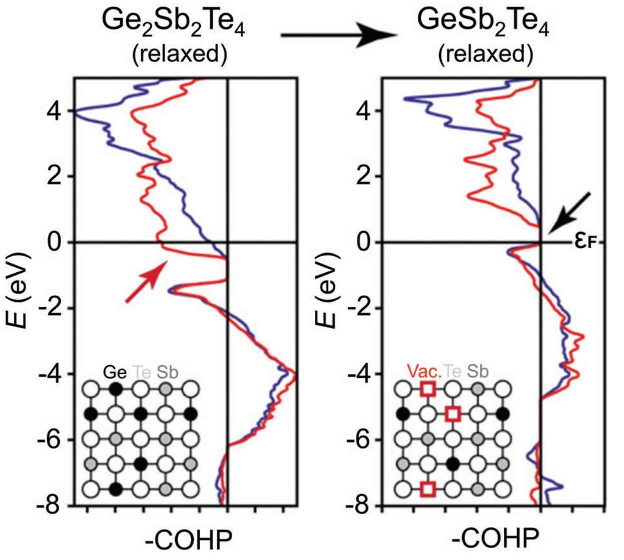

Figure 6. Crystal orbital Hamilton population (COHP) analysis of a fictional $Ge_2Sb_2Te_4$ phase (left) and the experimentally observed $GeSb_2Te_4$ phase (right). In $Ge_2Sb_2Te_4$, a significant occupation of antibonding states prevails (red arrow). On the contrary, these states are mostly depopulated in vacancy rich $GeSb_2Te_4$ (black arrow). Reproduced with permission.[61] Copyright 2019, WILEY-VCH.

in energy of carrier pockets not related by symmetry, hence enhancing the overall degeneracy.[71,72]

To a first approximation, the local atomic arrangement and the orbital character of the electronic states determine the energy dispersion relation within the Brillouin zone. The resulting bands also mirror the crystal symmetry. Due to the number of valence electrons (on average three per site) and the octahedral atomic arrangement, cubic IV–VI compounds have half-filled p-bands.[73] Such a coordination originates from the σ-bonds formed between valence p-electrons of neighboring atoms (see Figure 5). The valence band maximum and the conduction band minimum are both located at the L point of the Brillouin zone. Those states mostly exhibit VI p and IV p character, respectively, and acquire excess energy because of weak s–p hybridization. They are responsible for charge transport and exhibit a degeneracy of 4, due to the lower symmetry of the L point with respect to the point-group symmetry of the crystal. This corresponds to high valley degeneracy in octahedral-like group IV chalcogenides, which is found also in octahedral-like group V chalcogenides for similar reasons. For example, $N_V = 4$ in PbTe,[72] PbSe,[74] SnTe,[75–77] and GeTe[78,79] (recent papers report on $N_V = 6$ in GeTe[40,78,80]) and $N_V = 6$ in Bi_2Te_3.[81]

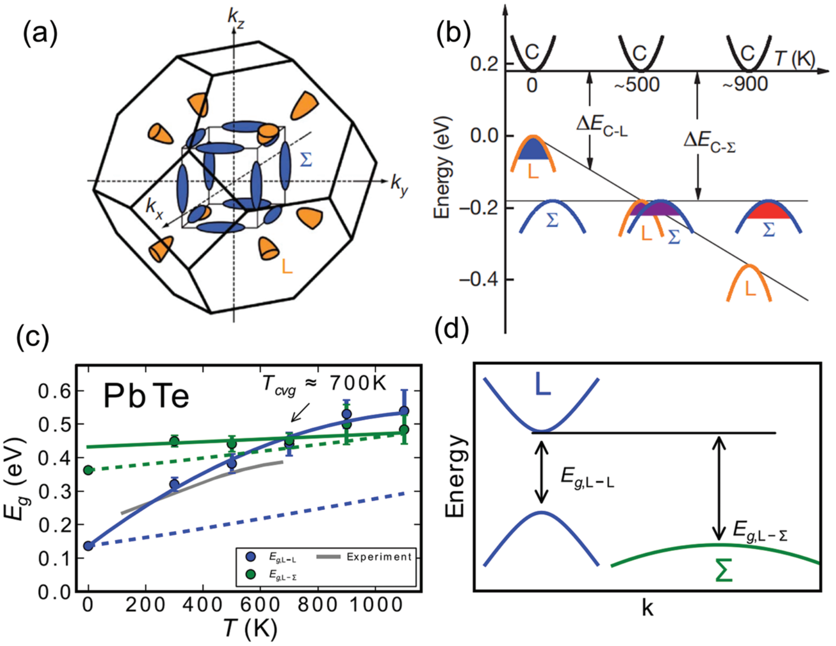

Figure 7. a) First Brillouin zone of PbTe showing the degenerate hole pockets centered at the L point (yellow) and along the Σ line (blue); b) Relative energy of the valence bands in $PbTe_{0.85}Se_{0.15}$. At ≈500 K the two valence bands converge; c) ab initio molecular dynamics calculation of the electron–phonon interaction and lattice expansion contributions to the temperature dependence of the bandgap in PbTe. Dashed lines represent the calculated contribution due to lattice expansion only; d) A near edge band structure diagram for PbTe. Insets (a) and (b) are reprinted with permission.[72] Copyright 2011 Macmillan Publishers Limited. Insets (c) and (d) are reproduced with permission.[86] Copyright 2013, AIP Publishing LLC.

In addition to the high valley degeneracy for the band extrema, the chalcogenides with octahedral-like structure listed in Table 1 often also possess a highly degenerate second valley lying not far below the top of the valence band. Thus, an increased orbital degeneracy can sometimes be realized by doping/alloying or changing the temperature. Taking PbTe as an example, there is a second valence state along the Σ line possessing a valley degeneracy of 12.[70,82] A schematic diagram of the L and Σ carrier pockets in the first Brillouin zone of PbTe is shown in **Figure 7**a. The energy separation between the L-band and the Σ-band is about 0.15 eV, making it possible to realize band convergence and hence an enlarged valley degeneracy by increasing the temperature to around 500 K (Figure 7b).[72] The increased bandgap with temperature also inhibits the excitation of minority carriers, promoting the high-temperature thermoelectric performance. One explanation for band convergence is based on thermal expansion, which leads to larger bond lengths and reduced orbital overlap. The resulting smaller s–p hybridization lowers the energy of the valence band at the L point, which approaches the Σ-band and leads to a larger bandgap.[83] Alternatively, some reports claim that the effect of thermal disorder on the Pb sublattice in Pb chalcogenides is responsible for the positive temperature coefficient for the bandgap.[84,85] Indeed, ab initio molecular dynamics calculations demonstrate that the bandgap increase due only to lattice expansion is much smaller than the experimentally observed results for PbTe (Figure 7c,d). Furthermore, these results indicate that also electron–phonon coupling contributes to the positive temperature coefficients of the bandgap.[85–87] A similar scenario is also observed in PbSe and PbS using the same methods, whose L- and Σ-bands converge at 900 and 1000 K, respectively.[86] The temperature of band convergence can also be estimated by the peak position in the measurement of Hall coefficient with temperature.[76–78,88–90] The existence of a relevant second band in PbTe was indeed first found by the temperature dependent Hall measurement.[91]

Temperature-induced band convergence cannot be realized if the energy separation between the top two valence bands is too large or the bandgap has a negative temperature coefficient. In these cases, doping or alloying can be adopted to modify the band structure and the position of Fermi energy, in order to achieve band convergence. This has been demonstrated in SnTe,[75,77,89,90,92] as well as in PbTe,[88,93–95] PbSe,[96] and GeTe[97] alloys.

4.2. Band Anisotropy

In addition to valley degeneracy, resonant impurity levels that create distortions in the DOS near the Fermi energy can be employed to enhance the Seebeck coefficient. This strategy has been successfully introduced in Tl-doped PbTe,[65] Al-doped PbSe,[98] In-doped SnTe,[99] In-doped GeTe,[100] and Sn-doped Bi_2Te_3.[101] However, even though the Seebeck coefficient is enhanced by the enlarged m_d^*, the carrier mobility is inevitably

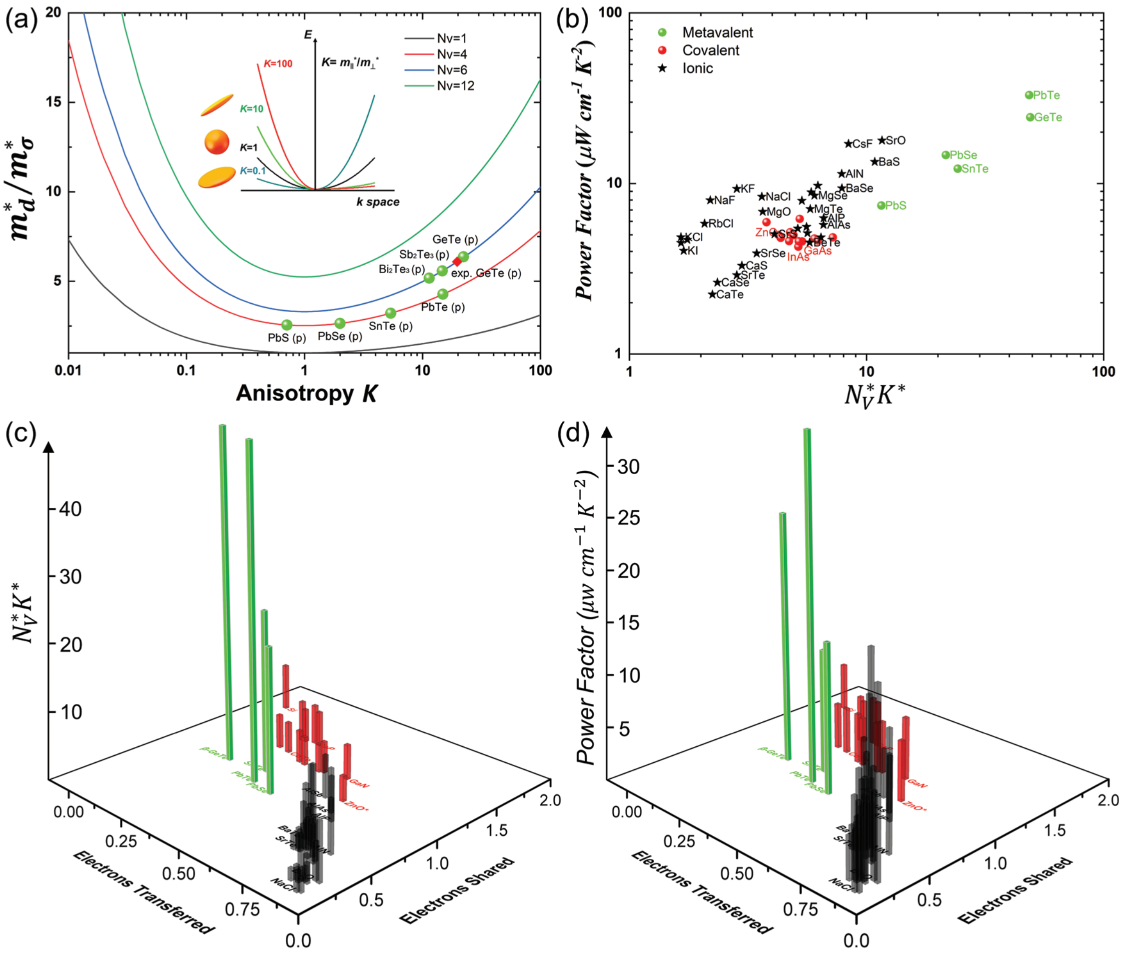

Figure 8. Effect of band anisotropy on the power factor for various solids. a) Ratio of $m_\mathrm{d}^*/m_\sigma^*$ as a function of band anisotropic factor K at different valley degeneracies. Data for octahedral chalcogenides are plotted. References: GeTe,[69] SnTe,[106] PbTe,[104] PbSe,[69] PbS,[107] Bi_2Te_3,[104] and Sb_2Te_3.[108] Inset is a schematic view of the valley anisotropy in the band structure diagram; Orange ellipsoids are the schematic Fermi surfaces with different wavevector k values; Inset is reproduced with permission.[109] Copyright 2018, Springer Nature; b) Maximum power factor for cubic compounds adopting different chemical bonding mechanisms as a function of the Fermi surface complexity factor, $N_\mathrm{V}^*K^*$; c) A 3D map using the basal plane of electrons transferred and electrons shared showing the value of $N_\mathrm{V}^*K^*$ and d) maximum power factor. Data sources of insets (b–d) are reproduced with permission.[105] Copyright 2017, Springer Nature.

reduced because of the heavier charge carriers and enhanced resonant scattering.[65,102]

Another approach to increase m_d^* is band flattening. Indeed, the effective mass tensor m^* is determined by the curvature of the energy dispersion relation at the band edge, according to $m^* = \hbar^2\,(d^2E/dk_i dk_j)^{-1}$. Heavier components will result in larger m_d^*. This has been realized in MnTe-doped PbTe[103] and Cu_2Se-doped PbSe[36] n-type chalcogenides. As a result, the power factor and zT values were enhanced.

It is important to bear in mind that the components of the effective mass tensor average differently to provide m_d^* and m_σ^*. As mentioned in Equations (1)–(7), the Seebeck coefficient is proportional to m_d^*, while the electrical conductivity is inversely proportional to m_σ^*. Then, the power factor depends on the electronic band structure via the ratio $m_\mathrm{d}^*/m_\sigma^*$[104]

$$\frac{m_\mathrm{d}^*}{m_\sigma^*} = (N_\mathrm{V})^{2/3}\,\frac{2m_\parallel^* + m_\perp^*}{3\left(m_\perp^*\right)^{1/3}\left(m_\parallel^*\right)^{2/3}} = (N_\mathrm{V})^{2/3}\,\frac{2K+1}{3K^{2/3}} \tag{8}$$

where K is the ratio between longitudinal and transverse effective masses, $K = m_\parallel^*/m_\perp^*$. As shown in **Figure** 8a, at a given valley degeneracy, the stronger deviation of K from 1, the larger the ratio of $m_\mathrm{d}^*/m_\sigma^*$. This enlarged anisotropy gives rise to a net enhancement of the power factor. Gibbs et al.[105] studied the effective mass and Fermi surface complexity factor for more than 2000 cubic compounds using ab initio band structure calculations. This Fermi surface complexity factor is defined as

$$N_\mathrm{V}^*K^* = \left(m_\mathrm{d}^*/m_\sigma^*\right)^{3/2} \tag{9}$$

Figure 8b illustrates the calculated maximum power factor versus $N_\mathrm{V}^*K^*$ for materials adopting metavalent, covalent, and ionic bonding. It is evident that the metavalent compounds possess a relative large Fermi surface complexity factor and higher maximum power factor than covalent and ionic compounds. By plotting $N_\mathrm{V}^*K^*$ and power factor onto the basal plane of electrons transferred and electrons shared, as shown in Figure 8c,d, it is very striking to find that the high values of $N_\mathrm{V}^*K^*$ and power factor concentrate on the green-coded metavalent bonding area.

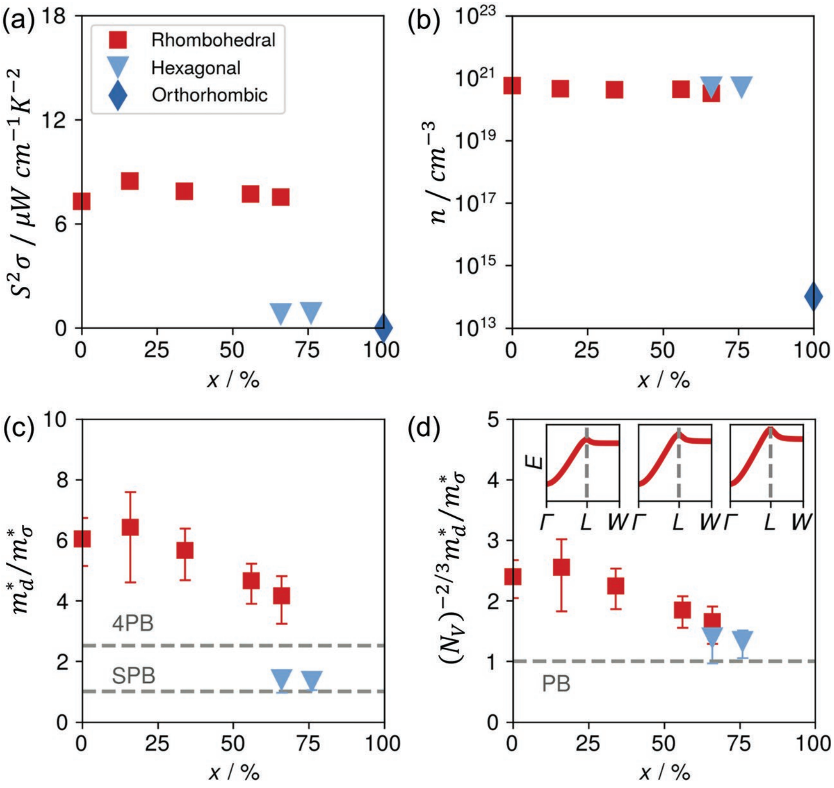

Figure 9. Electronic transport properties and effective masses in crystalline GeTe$_{1-x}$Se$_x$ alloys as a function of stoichiometry and crystal structure. a) Power factor; b) Carrier concentration; c) Ratio of m_d^*/m_σ^*. Ideal values for the single parabolic band (SPB) and the four parabolic band (4 PB) model are given as dashed lines for comparison; d) m_d^*/m_σ^* normalized to the valley degeneracy. Inset sketches the band structure with a gradual change of chemical composition and bonding. Reproduced with permission.[110] Copyright 2018, WILEY-VCH.

A larger band anisotropy is beneficial for the thermoelectric performance, since it allows to maximize thermoelectric performance. A systematic study of the band anisotropy and power factor for (GeTe)$_{1-x}$–(GeSe)$_x$ solid solution may help answer this question.[110] **Figure 9**a shows that with increasing the content of GeSe, the ternary alloy undergoes a phase transition from rhombohedral to hexagonal at $x > 0.65$, while the pure GeSe phase is orthorhombic. The phase transition from rhombohedral to hexagonal is accompanied also by a change of chemical bonding from metavalent to covalent as confirmed by previous studies.[55] The power factor of GeSe is negligible due to its ultralow carrier concentration. GeSe contains almost no cation vacancies and thus a very small hole carrier concentration, which has been explained using COHP in Section 3. While the power factor of the rhombohedral phase is much larger than that of the hexagonal phase, their carrier concentrations are almost the same, Figure 9b. Given a specific carrier concentration, the increased power factor should either stem from the increased band degeneracy or the strengthened band anisotropy, or both, as indicated by Equation (8). Figure 9c gives the ratio of m_d^*/m_σ^* with different GeSe contents. The value for the hexagonal phase is close to the prediction for a single-isotropic-parabolic-band model. However, the value for the rhombohedral phase strongly deviates from the predictions even for a four-isotropic-parabolic-bands model. This deviation implies that the valence band configuration of rhombohedral (GeTe)$_{1-x}$–(GeSe)$_x$ alloy is not consistent with assumption of isotropy. Instead, the extra enhancement of the power factor must stem from the band anisotropy. By fitting the experimental m_d^*/m_σ^* value of GeTe to the theoretical lines on Figure 8c (highlighted by a red diamond point), the band anisotropic factor K is found to be 20 for $N_V = 6$, which is very close to the calculated value of 22.[69] The band anisotropy decreases with increasing content of GeSe. Figure 9d shows the ratio of m_d^*/m_σ^* normalized to the contribution from band valley degeneracy. The reduced anisotropy within the rhombohedral phase upon increasing GeSe content is in line with a gradual change of band structure, as sketched in the insets of Figure 9d. The enlarged ratio between band effective mass and conductivity effective mass guarantees a net increase of power factor.

Such a change can be related to a change in bonding properties by means of the linear combination of atomic orbitals.[111] This method enables to model the band structure as function of local atomic environment, valence energies of the constituent atoms, and their mutual bond energies (matrix elements). By approximating the band structure of rhombohedral GeTe by its parent rock-salt crystal structure,[78,79] simple expressions for the electron energy at the high-symmetry points of the Brillouin zone can be found as function of bond parameters. It is assumed that the valence band maximum of rhombohedral GeTe is at degenerate T and L points.[78,79] Recent density functional theory (DFT) calculations imply that it could also be at the Σ-point.[18,106] Then, the trend of the effective mass tensor with respect to changes in bond parameters can be inferred from the corresponding changes in the bandwidths along the principal axes. This description has been successfully implemented by means of s–p^3 next-nearest-neighbor tight-binding model.[110] It has been shown that increasing s–p mixing between cation s and anion p states increases the bandwidth along Γ–L with respect to the one along L–W, hence reducing the ratio between longitudinal and transverse effective masses.[69] A similar effect is caused by larger ionicity, which leads to a shorter lattice constant and increased bond strength between adjacent p-orbitals in a σ-bonding configuration. This description enables predictive tuning of the effective mass tensor and explains the experimental data presented above. Indeed, progressive alloying of GeTe with GeSe gradually strengthens s–p hybridization and ionicity, resulting in a reduced band anisotropy at the L-point. Generally speaking, it can be deduced that the p-orbital nature of the states ensures anisotropic carrier pockets at the L point. Then, increasing bond energy between cation s and anion p states reduces such an anisotropy. The effective values of such bond energy can be controlled by stoichiometry and/or structural distortions. Indeed, stoichiometry with cation s states and anion p states closer in energy will have larger corresponding s–p mixing, while larger distortions will counteract the effect of large s–p mixing in order to prevent an excessive increase of electron energy at the L point, which would make the structure unstable. Then, materials whose trade-off between stoichiometry and distortion effects leads to small effective s–p matrix element should have the most anisotropic carrier pockets. Those include materials with metavalent bonding, for example, GeTe,[69,105,110] PbTe,[105,112] Bi_2Te_3,[113] and $AgBiSe_2$,[104] etc.

5. Intrinsically Low Lattice Thermal Conductivity

Besides tailoring the electronic band structure by bond engineering to enhance the power factor as discussed above, suppressing the thermal conductivity is another effective approach for enhanced zT. In the quantum-mechanical theory, sound waves are quasiparticles called phonons. The heat conduction through the medium is the propagation of entropy by electrons and phonons, i.e., κ_e and κ_l.[114] The thermal conductivity of the electrons κ_e is directly related to the electrical conductivity σ according to the Wiedemann Franz law, $\kappa_e = L\sigma T$, where L is the Lorenz number, being equal to 1.5×10^{-8} V^2 K^{-2} for nondegenerate semiconductors and 2.4×10^{-8} V^2 K^{-2} for degenerate semiconductors and metals. Since a decent σ is required for good thermoelectric materials, there is no efficient method to decrease κ_e while keeping a large σ. Thus, reducing κ_l is more important and straightforward. The lattice thermal conductivity can be described in the language of phonon propagation. A strong scattering of phonons leads to low lattice thermal conductivity. In bulk materials, κ_l is determined by[115]

$$\kappa_l = \frac{1}{3} c_V v_g^2 \tau_p \tag{10}$$

where c_V is the specific heat, v_g is the phonon group velocity, and τ_p is the phonon relaxation time. The value of c_V is determined by the Dulong–Petit law at high temperatures, which covers the application temperature range for most of the chalcogenide thermoelectrics. The phonon group velocity can be described by the spring-ball model, $v_g \approx \sqrt{F/M}$, where F is the force constant between atoms, characterizing the strength of chemical bond, M is the mass of atoms. Soft chemical bonds lead to a small value of F. The phonon relaxation time can be suppressed by introducing various scattering centers for phonons. The mean free path of phonons ($\bar{l} = v_g \tau_p$) lies in the range between a few angstroms up to several hundreds of nanometers. Thus, a more efficient phonon scattering process is achieved by introducing hierarchical structural defects, including atomic-scale point defects,[43,77,89,116] nanoscale dislocations,[8,54,75,95,117,118] mesoscale interfaces,[10,12,96,119,120] and precipitates.[76,94,118,119,121] Except for these extrinsic structural defects, the intrinsic property of the material, i.e., the anharmonicity is also responsible for the phonon–phonon scattering in the whole phonon frequency range.[35,41,122,123] We will separately discuss the role of soft chemical bonds and large anharmonicity on decreasing the lattice thermal conductivity in the following.

5.1. Soft Chemical Bond

The bond strength is closely related to the bulk modulus, the coordination numbers, the electron densities, and the bond lengths. **Figure 10** illustrates that all metavalently bonded materials possess low bulk modulus and low Debye temperatures, demonstrating that this is a soft chemical bond. Indeed, the data displayed in Figure 10 reveal that materials, which employ covalent (red) and ionic (black) bonding show relatively larger values of bulk modulus and Debye temperatures compared

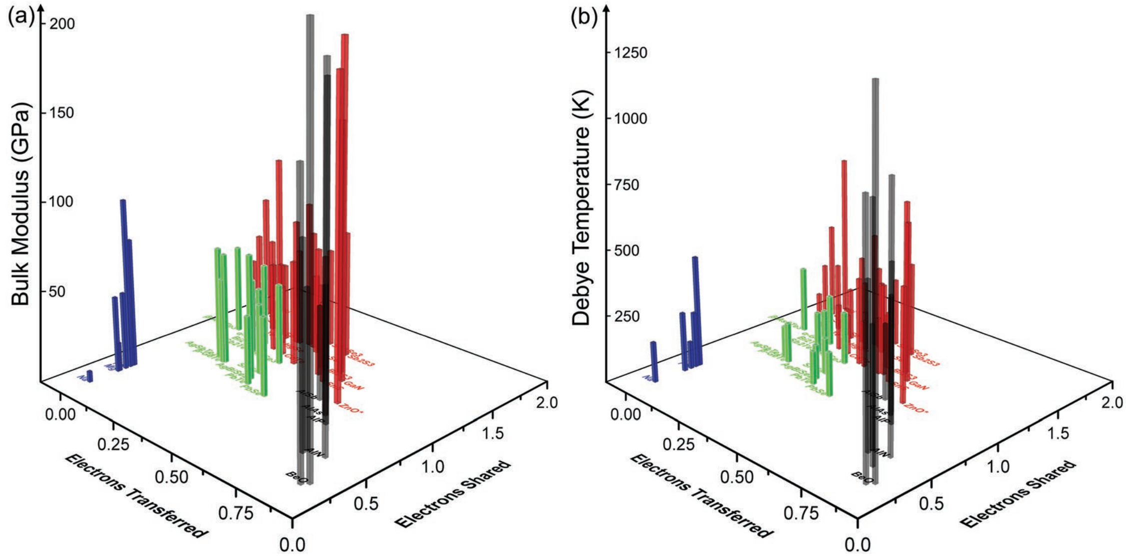

Figure 10. A map showing a) the bulk modulus and b) the Debye temperature of compounds adopting different bonding mechanisms. Green, red, black, and blue colors represent metavalent, covalent, ionic, and metallic bonding, respectively. Data are taken from ref. [108] A detailed list of all values is provided in Table S1 in the Supporting Information.

with the materials in the green area. There are additional arguments that support the idea of soft bonds for the materials in this region. It has been shown for example that upon crystallization of a typical chalcogenide used for phase change memory applications, i.e., the prototypical material $Ge_2Sb_2Te_5$, the optical phonon modes soften.[124] This is also compatible with the increased bond lengths between nearest neighbors which frequently accompany crystallization in chalcogenides utilized for phase change applications.[125] Employing bond length—bond strength correlations, which often adequately describe solids, provides further support for the existence of soft bonds in the octahedrally coordinated chalcogenides discussed here. One could simply argue that the presence of a single bonding electron (about one electron shared) between adjacent atoms simply corresponds to a smaller bond order than the case of an electron pair expected for a true covalent bond.

5.2. Large Anharmonicity

Even for a perfect crystal without any structural defects, the lattice thermal conductivity has a finite value because of the anharmonic phonon scattering by Umklapp processes. If we use the spring-ball model to describe the crystal lattice and its vibrations, in a harmonic system the spring constant is displacement independent and the interaction of phonons does not affect the net transport of heat. On the contrary, in an anharmonic system, the force is not proportional to the displacement. In other words, the atomic displacement induces a change in the spring constant. Under these conditions two phonons interact with each other, giving rise to a reflection of propagation velocity. This makes the net flow of phonons and entropy more difficult and reduces the lattice thermal conductivity.[114] The higher the anharmonicity, the lower the intrinsic lattice thermal conductivity. Generally, the anharmonicity is described by the Grüneisen parameter γ, which describes the relationship between phonon frequency and crystal volume change[126]

$$\gamma_{\mathrm{i}} = -\frac{V}{\omega_{\mathrm{i}}}\frac{\partial \omega_{\mathrm{i}}}{\partial V} \tag{11}$$

where ω_{i} is the phonon frequency and V is the crystal volume. For acoustic phonon dominated phonon scattering process, the lattice thermal conductivity can be expressed as[127]

$$\kappa_{\mathrm{l}} = A\frac{\bar{M}\Theta_{\mathrm{D}}^{3}\bar{V}^{1/3}}{\gamma^{2}n^{2/3}T} \tag{12}$$

Here, A is a collection of physical constants, $\bar{M}$ is the average mass of the atoms, Θ_{D} is the Debye temperature, $\bar{V}$ is the volume per atom, n is the number of atoms in the primitive unit cell, and T is the temperature. Two important parameters to reduce the thermal conductivity are the Debye temperature and the Grüneisen parameter. The γ^{-2} dependence of the lattice thermal conductivity for some covalent and ionic compounds with zincblende structure and metavalent compounds with rock-salt structure is illustrated in **Figure 11**. The large anharmonicity (large γ) is partly responsible for the intrinsically low lattice thermal conductivity of metavalently bonded materials.

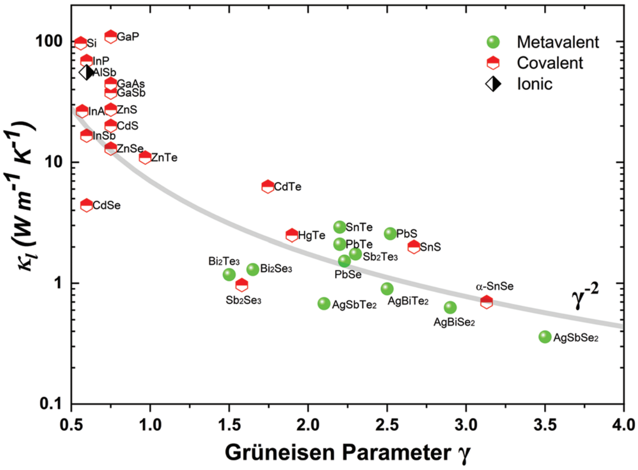

Figure 11. Dependence of lattice thermal conductivity κ_l on average Grüneisen parameter γ for materials adapting covalent, ionic, and metavalent bonding. Compounds which utilize metavalent bonding are characterized by particularly high Grüneisen parameters and hence low lattice thermal conductivities. Data points are taken from references for PbS,[128,129] PbSe,[96,128] PbTe,[130,131] SnS,[132] α-SnSe,[41,133] SnTe,[75,134] Sb_2Se_3,[46,135] Sb_2Te_3,[136,137] Bi_2Se_3,[46] Bi_2Te_3,[136,138] $AgSbSe_2$,[21,139] $AgSbTe_2$,[127] $AgBiSe_2$,[127,139] and $AgBiTe_2$.[139,140] Others are taken from ref. [70].

One can thus wonder, why metavalently bonded materials show such a large anharmonicity? Lee et al.[141] compared the lattice thermal conductivity of IV–VI, V_2VI_3, and V materials with that of zincblende III–V compounds using first-principles calculations. The results reveal that all metavalently bonded materials (note that "resonant bonding" is used in the reference article) exhibit a long-ranged interaction along the <100> direction. **Figure 12**a,b indicates that the long-ranged interaction is mainly coming from the p-electrons, while the polarization of s-electrons is short ranged and does not reach the fourth-nearest neighbor. Thus, the Pb-$6s^2$ lone-pair electrons have a negligible influence on the easily polarized electrons and intrinsically low lattice thermal conductivity of PbTe. As shown in Figure 3d, the Born effective charges for metavalently bonded materials are much larger than their nominal values, indicating a significant splitting of the longitudinal optical (LO) phonons and transverse optical (TO) phonons.[128] In addition, the highly delocalized p-electrons in a metavalent configuration produce a large electron-TO phonon coupling, causing optical phonon softening. In contrast, the octahedral coordinated NaCl shows very flat TO dispersions due to ionic bonding and localized electrons.[142] Even though the optical phonon modes are inefficient for heat transport due to their low group velocity, they can couple with the heat-carrying acoustic phonons by strong anharmonic scattering and, hence, lower the group velocity of acoustic phonons as well as an increase of the phase space for Umklapp phonon scattering processes. Therefore, a much lower lattice thermal conductivity is realized in metavalently bonded materials than III–V covalent compounds. The softened TO phonons and strong scattering with longitudinal acoustic (LA) phonons in PbTe have also been theoretically predicted by DFT calculations[143] and experimentally determined by inelastic neutron scattering as shown in Figure 12c,d.[122] Similarly large anharmonicities have also been found in other

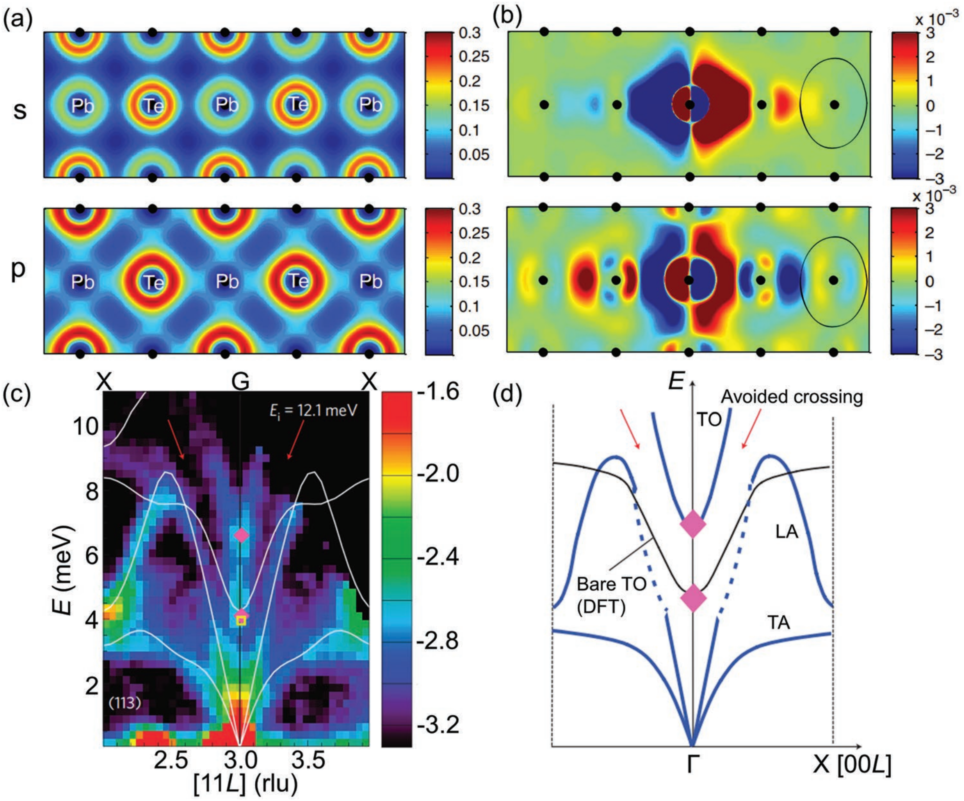

Figure 12. a) Electron density distribution at ground state for s- (top) and p-band electrons (bottom) in PbTe revealing a largely delocalized electron density of p-band electrons; b) Electron density polarization changes upon the displacement of the center atom. Here, the p-electrons show long-ranged polarization reaching the fourth-nearest neighbor as indicated by a circle, while s-electrons are rather localized; c) Phonon dispersions of PbTe obtained from inelastic neutron scattering at 300 K showing the avoided crossing of LA and TO phonon branches. The harmonic dispersions calculated by DFT are shown by white solid lines; d) Schematic representation of inset (c) with phonon dispersions as blue lines and the calculated bare TO branch as a solid black line. Insets (a) and (b) are reproduced with permission.[141] Copyright 2014, Macmillan Publishers Limited. Insets (c) and (d) are reproduced with permission.[122] Copyright 2011, Macmillan Publishers Limited.

metavalently bonded materials, e.g., SnTe,[131,134] I–V–VI_2,[123,127] and lead chalcogenides.[144]

6. Designing Chalcogenides with Superior Thermoelectric Performance

In the present manuscript, it has been argued that the outstanding thermoelectric performance of group IV–VI, V_2VI_3, and I–V–VI_2 chalcogenides can be understood from a chemical bonding perspective. The large optical dielectric constant, large Born effective charge, large TO mode Grüneisen parameter, large coordination number, and high “probability of multiple events” all indicate that these compounds adopt an unconventional bonding mechanism. This bonding mechanism can be located in a map, which separates solids according to the electrons shared and transferred between nearest neighbors. In this map, octahedrally coordinated chalcogenides show up in a special region, where materials show an unconventional, yet characteristic property portfolio. It has been shown here that this special bonding mechanism can be related to a large valley degeneracy, band convergence, as well as a large band anisotropy. This results in superior thermoelectric electronic transport properties, i.e., large power factors. In addition, this chemical bond is quite soft compared with covalent and ionic bonds. The long-ranged interactions of p-electrons produce a large coupling between electrons and TO phonons, causing optical phonon softening and a large anharmonicity. The soft chemical bond and a large anharmonicity lead to an intrinsically low thermal conductivity. These beneficial characteristics of metavalently bonded materials for thermoelectric are encoded in **Figure 13**. Hence, one can search for novel thermoelectrics employing the map. Yet, one can even go one step further. The map apparently also helps identifying property trends. As shown in Figure 3, there are clear property trends within the region of metavalently bonded materials. The TO mode Grüneisen parameter, for example, is highest in systems without a significant distortion away from perfect octahedral symmetry. Such systems are cubic and are located in the lower part of the green region. Combined with other property trends, this is providing some insight in which part of the green region of the map to look for superior thermoelectrics. Since the nature of chemical bonding can be tuned by alloying, we can thus optimize the thermoelectric properties by tailoring the chemical bonding mechanism.

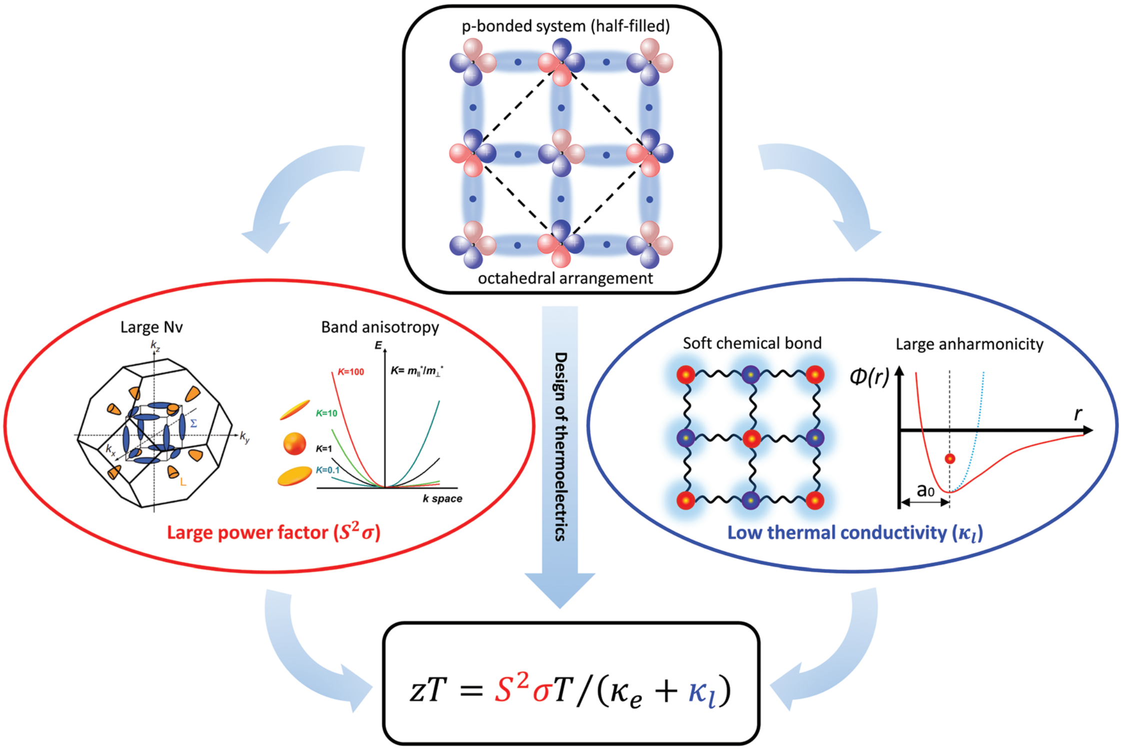

Figure 13. Relationship between chemical bonding and superior thermoelectric performance for octahedral-like chalcogenides. Compounds with metavalent bonding feature band structures, which often produce large band degeneracy and strong band anisotropy. This leads to an improved power factor. The bonding mechanism is also characterized by soft chemical bonds and large anharmonicity, which suppresses the lattice thermal conductivity. The superior thermoelectric performance of octahedrally coordinated chaclogenides is hence closely interwoven with their bonding mechanism. Schematic diagram for the large valley degeneracy is reproduced with permission.[72] Copyright 2011, Macmillan Publishers Limited; Schematic diagram for the band anisotropy is reproduced with permission.[109] Copyright 2018, Springer Nature.

Supporting Information

Supporting Information is available from the Wiley Online Library or from the author.

Acknowledgements

This work was supported by Deutsche Forschungsgemeinschaft (DFG) through SFB 917 "Nanoswitches." The research leading to these results has received funding from the Excellence Initiative (Distinguished Professorship). The authors are very grateful to Mathias Schumacher, Pavel Golub, and Jean-Yves Raty for providing some of the data utilized in Figures 2 and 3.

Conflict of Interest

The authors declare no conflict of interest.

Keywords

anharmonicity, band engineering, chalcogenide, metavalent bonding, thermoelectric

Received: June 17, 2019
Revised: July 9, 2019
Published online: August 15, 2019

[1] D. B. Gingerich, M. S. Mauter, *Environ. Sci. Technol.* **2015**, *49*, 8297.
[2] a) C. B. Vining, *Nature* **2001**, *413*, 577; b) L. Yang, Z.-G. Chen, M. S. Dargusch, J. Zou, *Adv. Energy Mater.* **2018**, *8*, 1701797.
[3] G. J. Snyder, E. S. Toberer, *Nat. Mater.* **2008**, *7*, 105.
[4] G. Tan, L. D. Zhao, M. G. Kanatzidis, *Chem. Rev.* **2016**, *116*, 12123.
[5] T. Zhu, Y. Liu, C. Fu, J. P. Heremans, G. J. Snyder, X. Zhao, *Adv. Mater.* **2017**, *29*, 1605884.
[6] D. J. Singh, in *Semiconductors and Semimetals* (Ed: T. M. Tritt), Vol. *70*, Elsevier, Amsterdam, Netherlands **2001**, p. 125.
[7] B. Lenoir, M. Cassart, J. P. Michenaud, H. Scherrer, S. Scherrer, *J. Phys. Chem. Solids* **1996**, *57*, 89.
[8] S. I. Kim, K. H. Lee, H. A. Mun, H. S. Kim, S. W. Hwang, J. W. Roh, D. J. Yang, W. H. Shin, X. S. Li, Y. H. Lee, *Science* **2015**, *348*, 109.
[9] H. J. Goldsmid, R. W. Douglas, *Br. J. Appl. Phys.* **1954**, *5*, 386.
[10] B. Poudel, Q. Hao, Y. Ma, Y. Lan, A. Minnich, B. Yu, X. Yan, D. Wang, A. Muto, D. Vashaee, X. Chen, J. Liu, M. S. Dresselhaus, G. Chen, Z. Ren, *Science* **2008**, *320*, 634.
[11] a) B. Zhu, Z.-Y. Huang, X.-Y. Wang, Y. Yu, L. Yang, N. Gao, Z.-G. Chen, F.-Q. Zu, *Nano Energy* **2017**, *42*, 8; b) B. Zhu, Y. Yu, X.-y. Wang, F.-q. Zu, Z.-y. Huang, *J. Mater. Sci.* **2017**, *52*, 8526.
[12] Y. Yu, D.-S. He, S. Zhang, O. Cojocaru-Mirédin, T. Schwarz, A. Stoffers, X.-Y. Wang, S. Zheng, B. Zhu, C. Scheu, D. Wu, J.-Q. He, M. Wuttig, Z.-Y. Huang, F.-Q. Zu, *Nano Energy* **2017**, *37*, 203.
[13] D.-Y. Chung, T. Hogan, P. Brazis, M. Rocci-Lane, C. Kannewurf, M. Bastea, C. Uher, M. G. Kanatzidis, *Science* **2000**, *287*, 1024.
[14] P. Ying, X. Li, Y. Wang, J. Yang, C. Fu, W. Zhang, X. Zhao, T. Zhu, *Adv. Funct. Mater.* **2017**, *27*, 1604145.

[15] A. D. LaLonde, Y. Pei, H. Wang, G. Jeffrey Snyder, *Mater. Today* **2011**, *14*, 526.
[16] Y. Xiao, L.-D. Zhao, *npj Quantum Mater.* **2018**, *3*, 55.
[17] W. Li, Y. Wu, S. Lin, Z. Chen, J. Li, X. Zhang, L. Zheng, Y. Pei, *ACS Energy Lett.* **2017**, *2*, 2349.
[18] M. Hong, J. Zou, Z. G. Chen, *Adv. Mater.* **2019**, *31*, 1807071.
[19] Z.-G. Chen, X. Shi, L.-D. Zhao, J. Zou, *Prog. Mater. Sci.* **2018**, *97*, 283.
[20] a) O. Cojocaru-Miredin, L. Abdellaoui, M. Nagli, S. Zhang, Y. Yu, C. Scheu, D. Raabe, M. Wuttig, Y. Amouyal, *ACS Appl. Mater. Interfaces* **2017**, *9*, 14779; b) L. Pan, D. Berardan, N. Dragoe, *J. Am. Chem. Soc.* **2013**, *135*, 4914; c) S. N. Guin, K. Biswas, *Chem. Mater.* **2013**, *25*, 3225.
[21] S. N. Guin, A. Chatterjee, D. S. Negi, R. Datta, K. Biswas, *Energy Environ. Sci.* **2013**, *6*, 2603.
[22] a) X. Shi, X. Wang, W. Li, Y. Pei, *Small Methods* **2018**, *2*, 1800022; b) H. Tamaki, H. K. Sato, T. Kanno, *Adv. Mater.* **2016**, *28*, 10182; c) S. Ohno, K. Imasato, S. Anand, H. Tamaki, S. D. Kang, P. Gorai, H. K. Sato, E. S. Toberer, T. Kanno, G. J. Snyder, *Joule* **2018**, *2*, 141.
[23] B. Sales, D. Mandrus, R. K. Williams, *Science* **1996**, *272*, 1325.
[24] G. Nolas, J. Cohn, G. Slack, S. Schujman, *Appl. Phys. Lett.* **1998**, *73*, 178.
[25] H. Liu, X. Shi, F. Xu, L. Zhang, W. Zhang, L. Chen, Q. Li, C. Uher, T. Day, G. J. Snyder, *Nat. Mater.* **2012**, *11*, 422.
[26] Y. L. Pei, H. Wu, D. Wu, F. Zheng, J. He, *J. Am. Chem. Soc.* **2014**, *136*, 13902.
[27] G. Joshi, H. Lee, Y. Lan, X. Wang, G. Zhu, D. Wang, R. W. Gould, D. C. Cuff, M. Y. Tang, M. S. Dresselhaus, G. Chen, Z. Ren, *Nano Lett.* **2008**, *8*, 4670.
[28] A. F. May, J.-P. Fleurial, G. J. Snyder, *Phys. Rev. B* **2008**, *78*, 125205.
[29] T. Zhu, C. Fu, H. Xie, Y. Liu, X. Zhao, *Adv. Energy Mater.* **2015**, *5*, 1500588.
[30] a) W. Zhang, R. Mazzarello, M. Wuttig, E. Ma, *Nat. Rev. Mater.* **2019**, *4*, 150; b) D. Lencer, M. Salinga, B. Grabowski, T. Hickel, J. Neugebauer, M. Wuttig, *Nat. Mater.* **2008**, *7*, 972.
[31] M. Wuttig, N. Yamada, *Nat. Mater.* **2007**, *6*, 824.
[32] H. Zhang, C.-X. Liu, X.-L. Qi, X. Dai, Z. Fang, S.-C. Zhang, *Nat. Phys.* **2009**, *5*, 438.
[33] J. Mao, Z. Liu, J. Zhou, H. Zhu, Q. Zhang, G. Chen, Z. Ren, *Adv. Phys.* **2018**, *67*, 69.
[34] L.-D. Zhao, G. Tan, S. Hao, J. He, Y. Pei, H. Chi, H. Wang, S. Gong, H. Xu, V. P. Dravid, C. Uher, G. J. Snyder, C. Wolverton, M. G. Kanatzidis, *Science* **2016**, *351*, 141.
[35] C. Chang, M. Wu, D. He, Y. Pei, C.-F. Wu, X. Wu, H. Yu, F. Zhu, K. Wang, Y. Chen, L. Huang, J.-F. Li, J. He, L.-D. Zhao, *Science* **2018**, *360*, 778.
[36] C. Zhou, Y. Yu, Y. K. Lee, O. Cojocaru-Mirédin, B. Yoo, S.-P. Cho, J. Im, M. Wuttig, T. Hyeon, I. Chung, *J. Am. Chem. Soc.* **2018**, *140*, 15535.
[37] S. LeBlanc, S. K. Yee, M. L. Scullin, C. Dames, K. E. Goodson, *Renewable Sustainable Energy Rev.* **2014**, *32*, 313.
[38] F. J. DiSalvo, *Science* **1999**, *285*, 703.
[39] Y. Wu, Z. Chen, P. Nan, F. Xiong, S. Lin, X. Zhang, Y. Chen, L. Chen, B. Ge, Y. Pei, *Joule* **2019**, *3*, 1276.
[40] J. Li, X. Zhang, Z. Chen, S. Lin, W. Li, J. Shen, I. T. Witting, A. Faghaninia, Y. Chen, A. Jain, L. Chen, G. J. Snyder, Y. Pei, *Joule* **2018**, *2*, 976.
[41] L. D. Zhao, S. H. Lo, Y. Zhang, H. Sun, G. Tan, C. Uher, C. Wolverton, V. P. Dravid, M. G. Kanatzidis, *Nature* **2014**, *508*, 373.
[42] a) C. Han, Q. Sun, Z. Li, S. X. Dou, *Adv. Energy Mater.* **2016**, *6*, 1600498; b) L.-D. Zhao, V. P. Dravid, M. G. Kanatzidis, *Energy Environ. Sci.* **2014**, *7*, 251; c) X. Shi, L. Chen, C. Uher, *Int. Mater. Rev.* **2016**, *61*, 379; d) M. G. Kanatzidis, *Chem. Mater.* **2010**, *22*, 648; e) J. G. Park, Y. H. Lee, *Curr. Appl. Phys.* **2016**, *16*, 1202; f) L.-D. Zhao, C. Chang, G. Tan, M. G. Kanatzidis, *Energy Environ. Sci.* **2016**, *9*, 3044.
[43] T. Zhu, L. Hu, X. Zhao, J. He, *Adv. Sci.* **2016**, *3*, 1600004.
[44] S. Perumal, S. Roychowdhury, D. S. Negi, R. Datta, K. Biswas, *Chem. Mater.* **2015**, *27*, 7171.
[45] M. Yan, X. Tan, Z. Huang, G. Liu, P. Jiang, X. Bao, *J. Mater. Chem. A* **2018**, *6*, 8215.
[46] X. Liu, D. Wang, H. Wu, J. Wang, Y. Zhang, G. Wang, S. J. Pennycook, L.-D. Zhao, *Adv. Funct. Mater.* **2019**, *29*, 1806558.
[47] K. Biswas, L.-D. Zhao, M. G. Kanatzidis, *Adv. Energy Mater.* **2012**, *2*, 634.
[48] J. O. Sofo, G. D. Mahan, *Phys. Rev. B* **1994**, *49*, 4565.
[49] M. Wuttig, V. L. Deringer, X. Gonze, C. Bichara, J. Y. Raty, *Adv. Mater.* **2018**, *30*, 1803777.
[50] J. Y. Raty, M. Schumacher, P. Golub, V. L. Deringer, C. Gatti, M. Wuttig, *Adv. Mater.* **2019**, *31*, 1806280.
[51] P. Golub, A. I. Baranov, *J. Chem. Phys.* **2016**, *145*, 154107.
[52] G. N. Lewis, *J. Am. Chem. Soc.* **1916**, *38*, 762.
[53] B. Gault, *Appl. Microsc.* **2016**, *46*, 117.
[54] Y. Yu, S. Zhang, A. M. Mio, B. Gault, A. Sheskin, C. Scheu, D. Raabe, F. Zu, M. Wuttig, Y. Amouyal, O. Cojocaru-Miredin, *ACS Appl. Mater. Interfaces* **2018**, *10*, 3609.
[55] M. Zhu, O. Cojocaru-Miredin, A. M. Mio, J. Keutgen, M. Kupers, Y. Yu, J. Y. Cho, R. Dronskowski, M. Wuttig, *Adv. Mater.* **2018**, *30*, 1706735.
[56] A. Zevalkink, D. M. Smiadak, J. L. Blackburn, A. J. Ferguson, M. L. Chabinyc, O. Delaire, J. Wang, K. Kovnir, J. Martin, L. T. Schelhas, T. D. Sparks, S. D. Kang, M. T. Dylla, G. J. Snyder, B. R. Ortiz, E. S. Toberer, *Appl. Phys. Rev.* **2018**, *5*, 021303.
[57] R. Dronskowski, P. E. Blöchl, *J. Phys. Chem.* **1993**, *97*, 8617.
[58] A. Edwards, A. Pineda, P. Schultz, M. Martin, A. Thompson, H. Hjalmarson, C. Umrigar, *Phys. Rev. B* **2006**, *73*, 045210.
[59] M. Wuttig, D. Lusebrink, D. Wamwangi, W. Welnic, M. Gillessen, R. Dronskowski, *Nat. Mater.* **2007**, *6*, 122.
[60] D. Lencer, M. Salinga, M. Wuttig, *Adv. Mater.* **2011**, *23*, 2030.
[61] P. M. Konze, R. Dronskowski, V. L. Deringer, *Phys. Status Solidi RRL* **2019**, *13*, 1800579.
[62] a) V. L. Deringer, W. Zhang, M. Lumeij, S. Maintz, M. Wuttig, R. Mazzarello, R. Dronskowski, *Angew. Chem., Int. Ed.* **2014**, *53*, 10817; b) U. V. Waghmare, N. A. Spaldin, H. C. Kandpal, R. Seshadri, *Phys. Rev. B* **2003**, *67*, 125111.
[63] V. L. Deringer, R. P. Stoffel, M. Wuttig, R. Dronskowski, *Chem. Sci.* **2015**, *6*, 5255.
[64] F. Rao, K. Ding, Y. Zhou, Y. Zheng, M. Xia, S. Lv, Z. Song, S. Feng, I. Ronneberger, R. Mazzarello, W. Zhang, E. Ma, *Science* **2017**, *358*, 1423.
[65] J. P. Heremans, V. Jovovic, E. S. Toberer, A. Saramat, K. Kurosaki, A. Charoenphakdee, S. Yamanaka, G. J. Snyder, *Science* **2008**, *321*, 554.
[66] S. Wang, J. Yang, L. Wu, P. Wei, W. Zhang, J. Yang, *Adv. Funct. Mater.* **2015**, *25*, 6660.
[67] a) J. P. Heremans, C. M. Thrush, D. T. Morelli, *J. Appl. Phys.* **2005**, *98*, 063703; b) A. J. Minnich, M. S. Dresselhaus, Z. F. Ren, G. Chen, *Energy Environ. Sci.* **2009**, *2*, 466; c) J. Li, Q. Tan, J.-F. Li, D.-W. Liu, F. Li, Z.-Y. Li, M. Zou, K. Wang, *Adv. Funct. Mater.* **2013**, *23*, 4317.
[68] D. Parker, D. J. Singh, *Phys. Rev. B* **2010**, *82*, 035204.
[69] X. Chen, D. Parker, D. J. Singh, *Sci. Rep.* **2013**, *3*, 3168.
[70] W. G. Zeier, A. Zevalkink, Z. M. Gibbs, G. Hautier, M. G. Kanatzidis, G. J. Snyder, *Angew. Chem., Int. Ed.* **2016**, *55*, 6826.
[71] W. Liu, X. Tan, K. Yin, H. Liu, X. Tang, J. Shi, Q. Zhang, C. Uher, *Phys. Rev. Lett.* **2012**, *108*, 166601.
[72] Y. Pei, X. Shi, A. LaLonde, H. Wang, L. Chen, G. J. Snyder, *Nature* **2011**, *473*, 66.
[73] K. Shportko, S. Kremers, M. Woda, D. Lencer, J. Robertson, M. Wuttig, *Nat. Mater.* **2008**, *7*, 653.

[74] H. Wang, Y. Pei, A. D. LaLonde, G. J. Snyder, *Adv. Mater.* **2011**, *23*, 1366.
[75] F. Guo, B. Cui, Y. Liu, X. Meng, J. Cao, Y. Zhang, R. He, W. Liu, H. Wu, S. J. Pennycook, W. Cai, J. Sui, *Small* **2018**, *14*, 1802615.
[76] H. Wu, C. Chang, D. Feng, Y. Xiao, X. Zhang, Y. Pei, L. Zheng, D. Wu, S. Gong, Y. Chen, J. He, M. G. Kanatzidis, L.-D. Zhao, *Energy Environ. Sci.* **2015**, *8*, 3298.
[77] J. Tang, B. Gao, S. Lin, J. Li, Z. Chen, F. Xiong, W. Li, Y. Chen, Y. Pei, *Adv. Funct. Mater.* **2018**, *28*, 1803586.
[78] D. Wu, L. D. Zhao, S. Hao, Q. Jiang, F. Zheng, J. W. Doak, H. Wu, H. Chi, Y. Gelbstein, C. Uher, C. Wolverton, M. Kanatzidis, J. He, *J. Am. Chem. Soc.* **2014**, *136*, 11412.
[79] a) Y. Chen, C. M. Jaworski, Y. B. Gao, H. Wang, T. J. Zhu, G. J. Snyder, J. P. Heremans, X. B. Zhao, *New J. Phys.* **2014**, *16*, 013057; b) R. Shaltaf, E. Durgun, J. Y. Raty, P. Ghosez, X. Gonze, *Phys. Rev. B* **2008**, *78*, 205203.
[80] M. Hong, Y. Wang, W. Liu, S. Matsumura, H. Wang, J. Zou, Z.-G. Chen, *Adv. Energy Mater.* **2018**, *8*, 1801837.
[81] H. Goldsmid, *Thermoelectric Refrigeration*, Springer, Berlin, Germany **2013**.
[82] E. A. Albanesi, C. M. I. Okoye, C. O. Rodriguez, E. L. Peltzer y Blanca, A. G. Petukhov, *Phys. Rev. B* **2000**, *61*, 16589.
[83] S.-H. Wei, A. Zunger, *Phys. Rev. B* **1997**, *55*, 13605.
[84] a) Y. Zhang, X. Ke, P. R. Kent, J. Yang, C. Chen, *Phys. Rev. Lett.* **2011**, *107*, 175503; b) E. S. Božin, C. D. Malliakas, P. Souvatzis, T. Proffen, N. A. Spaldin, M. G. Kanatzidis, S. J. L. Billinge, *Science* **2010**, *330*, 1660.
[85] H. Kim, M. Kaviany, *Phys. Rev. B* **2012**, *86*, 045213.
[86] Z. M. Gibbs, H. Kim, H. Wang, R. L. White, F. Drymiotis, M. Kaviany, G. Jeffrey Snyder, *Appl. Phys. Lett.* **2013**, *103*, 262109.
[87] M. Baleva, T. Georgiev, G. J. J. o. P. C. M. Lashkarev, *J. Phys.: Condens. Matter* **1990**, *2*, 2935.
[88] G. Tan, F. Shi, S. Hao, L.-D. Zhao, H. Chi, X. Zhang, C. Uher, C. Wolverton, V. P. Dravid, M. G. Kanatzidis, *Nat. Commun.* **2016**, *7*, 12167.
[89] W. Li, L. Zheng, B. Ge, S. Lin, X. Zhang, Z. Chen, Y. Chang, Y. Pei, *Adv. Mater.* **2017**, *29*, 1605887.
[90] G. Tan, F. Shi, J. W. Doak, H. Sun, L.-D. Zhao, P. Wang, C. Uher, C. Wolverton, V. P. Dravid, M. G. Kanatzidis, *Energy Environ. Sci.* **2015**, *8*, 267.
[91] R. S. Allgaier, *J. Appl. Phys.* **1961**, *32*, 2185.
[92] G. Tan, F. Shi, S. Hao, H. Chi, L. D. Zhao, C. Uher, C. Wolverton, V. P. Dravid, M. G. Kanatzidis, *J. Am. Chem. Soc.* **2015**, *137*, 5100.
[93] Y. Pei, G. Tan, D. Feng, L. Zheng, Q. Tan, X. Xie, S. Gong, Y. Chen, J.-F. Li, J. He, M. G. Kanatzidis, L.-D. Zhao, *Adv. Energy Mater.* **2017**, *7*, 1601450.
[94] L. D. Zhao, H. J. Wu, S. Q. Hao, C. I. Wu, X. Y. Zhou, K. Biswas, J. Q. He, T. P. Hogan, C. Uher, C. Wolverton, V. P. Dravid, M. G. Kanatzidis, *Energy Environ. Sci.* **2013**, *6*, 3346.
[95] Z. Chen, Z. Jian, W. Li, Y. Chang, B. Ge, R. Hanus, J. Yang, Y. Chen, M. Huang, G. J. Snyder, Y. Pei, *Adv. Mater.* **2017**, *29*, 1606768.
[96] L. D. Zhao, S. Hao, S. H. Lo, C. I. Wu, X. Zhou, Y. Lee, H. Li, K. Biswas, T. P. Hogan, C. Uher, C. Wolverton, V. P. Dravid, M. G. Kanatzidis, *J. Am. Chem. Soc.* **2013**, *135*, 7364.
[97] a) M. Hong, Y. Wang, T. Feng, Q. Sun, S. Xu, S. Matsumura, S. T. Pantelides, J. Zou, Z. G. Chen, *J. Am. Chem. Soc.* **2019**, *141*, 1742; b) M. Hong, Z. G. Chen, L. Yang, Y. C. Zou, M. S. Dargusch, H. Wang, J. Zou, *Adv. Mater.* **2018**, *30*, 1705942.
[98] Q. Zhang, H. Wang, W. Liu, H. Wang, B. Yu, Q. Zhang, Z. Tian, G. Ni, S. Lee, K. Esfarjani, G. Chen, Z. Ren, *Energy Environ. Sci.* **2012**, *5*, 5246.
[99] L. Wang, X. Tan, G. Liu, J. Xu, H. Shao, B. Yu, H. Jiang, S. Yue, J. Jiang, *ACS Energy Lett.* **2017**, *2*, 1203.
[100] L. Wu, X. Li, S. Wang, T. Zhang, J. Yang, W. Zhang, L. Chen, J. Yang, *NPG Asia Mater.* **2017**, *9*, e343.
[101] C. M. Jaworski, J. P. Heremans, *Phys. Rev. B* **2009**, *80*, 233201.
[102] J. P. Heremans, B. Wiendlocha, A. M. Chamoire, *Energy Environ. Sci.* **2012**, *5*, 5510.
[103] Y. Xiao, H. Wu, J. Cui, D. Wang, L. Fu, Y. Zhang, Y. Chen, J. He, S. J. Pennycook, L.-D. Zhao, *Energy Environ. Sci.* **2018**, *11*, 2486.
[104] D. S. Parker, A. F. May, D. J. Singh, *Phys. Rev. Appl.* **2015**, *3*, 064003.
[105] Z. M. Gibbs, F. Ricci, G. Li, H. Zhu, K. Persson, G. Ceder, G. Hautier, A. Jain, G. J. Snyder, *npj Comput. Mater.* **2017**, *3*, 8.
[106] J. Li, Z. Chen, X. Zhang, Y. Sun, J. Yang, Y. Pei, *NPG Asia Mater.* **2017**, *9*, e353.
[107] S. Hao, F. Shi, V. P. Dravid, M. G. Kanatzidis, C. Wolverton, *Chem. Mater.* **2016**, *28*, 3218.
[108] O. Madelung, *Semiconductors: Data Handbook*, Springer Science & Business Media, Berlin, Germany **2012**.
[109] J. Xin, Y. Tang, Y. Liu, X. Zhao, H. Pan, T. Zhu, *npj Quantum Mater.* **2018**, *3*, 9.
[110] M. Cagnoni, D. Fuhren, M. Wuttig, *Adv. Mater.* **2018**, *30*, 1801787.
[111] R. Hoffmann, *Angew. Chem., Int. Ed. Engl.* **1987**, *26*, 846.
[112] D. Parker, X. Chen, D. J. Singh, *Phys. Rev. Lett.* **2013**, *110*, 146601.
[113] S. K. Mishra, S. Satpathy, O. Jepsen, *J. Phys.: Condens. Matter* **1997**, *9*, 461.
[114] J. P. Heremans, *Nat. Phys.* **2015**, *11*, 990.
[115] Z. Chen, X. Zhang, Y. Pei, *Adv. Mater.* **2018**, *30*, 1705617.
[116] a) X. Zhang, J. Li, X. Wang, Z. Chen, J. Mao, Y. Chen, Y. Pei, *J. Am. Chem. Soc.* **2018**, *140*, 15883; b) M. Steele, F. Rosi, *J. Appl. Phys.* **1958**, *29*, 1517; c) K. S. Siegert, F. R. Lange, E. R. Sittner, H. Volker, C. Schlockermann, T. Siegrist, M. Wuttig, *Rep. Prog. Phys.* **2015**, *78*, 013001; d) L. Fu, M. Yin, D. Wu, W. Li, D. Feng, L. Huang, J. He, *Energy Environ. Sci.* **2017**, *10*, 2030; e) D. Wu, L. Wu, D. He, L.-D. Zhao, W. Li, M. Wu, M. Jin, J. Xu, J. Jiang, L. Huang, Y. Zhu, M. G. Kanatzidis, J. He, *Nano Energy* **2017**, *35*, 321; f) L. Hu, T. Zhu, X. Liu, X. Zhao, *Adv. Funct. Mater.* **2014**, *24*, 5211.
[117] a) H.-S. Kim, S. D. Kang, Y. Tang, R. Hanus, G. Jeffrey Snyder, *Mater. Horiz.* **2016**, *3*, 234; b) Y. Pan, U. Aydemir, J. A. Grovogui, I. T. Witting, R. Hanus, Y. Xu, J. Wu, C. F. Wu, F. H. Sun, H. L. Zhuang, J. F. Dong, J. F. Li, V. P. Dravid, G. J. Snyder, *Adv. Mater.* **2018**, *30*, 1802016; c) Z. Chen, B. Ge, W. Li, S. Lin, J. Shen, Y. Chang, R. Hanus, G. J. Snyder, Y. Pei, *Nat. Commun.* **2017**, *8*, 13828.
[118] C. Zhou, Y. K. Lee, J. Cha, B. Yoo, S. P. Cho, T. Hyeon, I. Chung, *J. Am. Chem. Soc.* **2018**, *140*, 9282.
[119] a) J. He, I. D. Blum, H. Q. Wang, S. N. Girard, J. Doak, L. D. Zhao, J. C. Zheng, G. Casillas, C. Wolverton, M. Jose-Yacaman, D. N. Seidman, M. G. Kanatzidis, V. P. Dravid, *Nano Lett.* **2012**, *12*, 5979; b) K. Biswas, J. He, Q. Zhang, G. Wang, C. Uher, V. P. Dravid, M. G. Kanatzidis, *Nat. Chem.* **2011**, *3*, 160.
[120] a) X.-y. Wang, J. Yu, R.-f. Zhao, B. Zhu, N. Gao, B. Xiang, Y. Yu, K.-m. Zhang, Z.-y. Huang, F.-q. Zu, *J. Phys. Chem. Solids* **2019**, *124*, 281; b) X. Y. Wang, H. J. Wang, B. Xiang, L. W. Fu, H. Zhu, D. Chai, B. Zhu, Y. Yu, N. Gao, Z. Y. Huang, F. Q. Zu, *ACS Appl. Mater. Interfaces* **2018**, *10*, 23277; c) H. Mun, S.-M. Choi, K. H. Lee, S. W. Kim, *ChemSusChem* **2015**, *8*, 2312; d) D. L. Medlin, G. J. Snyder, *Curr. Opin. Colloid Interface Sci.* **2009**, *14*, 226.
[121] a) K. Ahn, K. Biswas, J. He, I. Chung, V. Dravid, M. G. Kanatzidis, *Energy Environ. Sci.* **2013**, *6*, 1529; b) L.-D. Zhao, X. Zhang, H. Wu, G. Tan, Y. Pei, Y. Xiao, C. Chang, D. Wu, H. Chi, L. Zheng, *J. Am. Chem. Soc.* **2016**, *138*, 2366; c) D. Wu, L.-D. Zhao, F. Zheng, L. Jin, M. G. Kanatzidis, J. He, *Adv. Mater.* **2016**, *28*, 2737; d) K. F. Hsu, S. Loo, F. Guo, W. Chen, J. S. Dyck, C. Uher, T. Hogan, E. K. Polychroniadis, M. G. Kanatzidis, *Science* **2004**, *303*, 818; e) D. Wu, L.-D. Zhao, X. Tong, W. Li, L. Wu, Q. Tan,

Y. Pei, L. Huang, J.-F. Li, Y. Zhu, M. G. Kanatzidis, J. He, *Energy Environ. Sci.* **2015**, *8*, 2056.
[122] O. Delaire, J. Ma, K. Marty, A. F. May, M. A. McGuire, M. H. Du, D. J. Singh, A. Podlesnyak, G. Ehlers, M. D. Lumsden, B. C. Sales, *Nat. Mater.* **2011**, *10*, 614.
[123] J. Ma, O. Delaire, A. F. May, C. E. Carlton, M. A. McGuire, L. H. VanBebber, D. L. Abernathy, G. Ehlers, T. Hong, A. Huq, W. Tian, V. M. Keppens, Y. Shao-Horn, B. C. Sales, *Nat. Nanotechnol.* **2013**, *8*, 445.
[124] T. Matsunaga, N. Yamada, R. Kojima, S. Shamoto, M. Sato, H. Tanida, T. Uruga, S. Kohara, M. Takata, P. Zalden, G. Bruns, I. Sergueev, H. C. Wille, R. P. Hermann, M. Wuttig, *Adv. Funct. Mater.* **2011**, *21*, 2232.
[125] J. Y. Raty, W. Zhang, J. Luckas, C. Chen, R. Mazzarello, C. Bichara, M. Wuttig, *Nat. Commun.* **2015**, *6*, 7467.
[126] C. Chang, L.-D. Zhao, *Mater. Today Phys.* **2018**, *4*, 50.
[127] D. T. Morelli, V. Jovovic, J. P. Heremans, *Phys. Rev. Lett.* **2008**, *101*, 035901.
[128] Y. Zhang, X. Ke, C. Chen, J. Yang, P. R. C. Kent, *Phys. Rev. B* **2009**, *80*, 024304.
[129] L. D. Zhao, S. H. Lo, J. He, H. Li, K. Biswas, J. Androulakis, C. I. Wu, T. P. Hogan, D. Y. Chung, V. P. Dravid, M. G. Kanatzidis, *J. Am. Chem. Soc.* **2011**, *133*, 20476.
[130] B. Houston, R. E. Strakna, H. S. Belson, *J. Appl. Phys.* **1968**, *39*, 3913.
[131] C. W. Li, J. Ma, H. B. Cao, A. F. May, D. L. Abernathy, G. Ehlers, C. Hoffmann, X. Wang, T. Hong, A. Huq, O. Gourdon, O. Delaire, *Phys. Rev. B* **2014**, *90*, 214303.
[132] W. He, D. Wang, J.-F. Dong, Y. Qiu, L. Fu, Y. Feng, Y. Hao, G. Wang, J. Wang, C. Liu, J.-F. Li, J. He, L.-D. Zhao, *J. Mater. Chem. A* **2018**, *6*, 10048.
[133] Y. Xiao, C. Chang, Y. Pei, D. Wu, K. Peng, X. Zhou, S. Gong, J. He, Y. Zhang, Z. Zeng, L.-D. Zhao, *Phys. Rev. B* **2016**, *94*, 125203.
[134] A. Banik, T. Ghosh, R. Arora, M. Dutta, J. Pandey, S. Acharya, A. Soni, U. V. Waghmare, K. Biswas, *Energy Environ. Sci.* **2019**, *12*, 589.
[135] S. Wang, Y. Sun, J. Yang, B. Duan, L. Wu, W. Zhang, J. Yang, *Energy Environ. Sci.* **2016**, *9*, 3436.
[136] X. Chen, H. D. Zhou, A. Kiswandhi, I. Miotkowski, Y. P. Chen, P. A. Sharma, A. L. Lima Sharma, M. A. Hekmaty, D. Smirnov, Z. Jiang, *Appl. Phys. Lett.* **2011**, *99*, 261912.
[137] L. P. Hu, T. J. Zhu, X. Q. Yue, X. H. Liu, Y. G. Wang, Z. J. Xu, X. B. Zhao, *Acta Mater.* **2015**, *85*, 270.
[138] W. Liu, K. C. Lukas, K. McEnaney, S. Lee, Q. Zhang, C. P. Opeil, G. Chen, Z. Ren, *Energy Environ. Sci.* **2013**, *6*, 552.
[139] M. D. Nielsen, V. Ozolins, J. P. Heremans, *Energy Environ. Sci.* **2013**, *6*, 570.
[140] Y. Takigawa, T. Imoto, T. Sakakibara, K. Kurosawa, *MRS Proc.* **1998**, *545*, 105.
[141] S. Lee, K. Esfarjani, T. Luo, J. Zhou, Z. Tian, G. Chen, *Nat. Commun.* **2014**, *5*, 3525.
[142] G. Raunio, L. Almqvist, R. Stedman, *Phys. Rev.* **1969**, *178*, 1496.
[143] a) J. An, A. Subedi, D. J. Singh, *Solid State Commun.* **2008**, *148*, 417; b) T. Shiga, J. Shiomi, J. Ma, O. Delaire, T. Radzynski, A. Lusakowski, K. Esfarjani, G. Chen, *Phys. Rev. B* **2012**, *85*, 155203.
[144] a) J. M. Skelton, S. C. Parker, A. Togo, I. Tanaka, A. Walsh, *Phys. Rev. B* **2014**, *89*, 205203; b) M. E. Manley, O. Hellman, N. Shulumba, A. F. May, P. J. Stonaha, J. W. Lynn, V. O. Garlea, A. Alatas, R. P. Hermann, J. D. Budai, H. Wang, B. C. Sales, A. J. Minnich, *Nat. Commun.* **2019**, *10*, 1928.